Jpn J Radiol (2014) 32:138–144
DOI 10.1007/s11604-013-0276-7

ORIGINAL ARTICLE

Analysis of early phase [^{11}C]BF-227 PET, and its application for anatomical standardization of late-phase images for 3D-SSP analysis

Tomohiro Kaneta · Nobuyuki Okamura · Akira Arai · Kentaro Takanami · Katsutoshi Furukawa · Manabu Tashiro · Shozo Furumoto · Ren Iwata · Shoki Takahashi · Hiroyuki Arai · Kazuhiko Yanai · Yukitsuka Kudo

Received: 14 August 2013 / Accepted: 22 December 2013 / Published online: 10 January 2014

Abstract
Purpose To examine the usefulness of the early phase [^{11}C]BF-227 positron emission tomography (PET) for (1) conferring additional diagnostic value by providing perfusion-like information and (2) obtaining the appropriate anatomical standardization (AS) using three-dimensional stereotactic surface projection (3D-SSP) method.
Methods This study included 20 mild cognitive impairment (MCI), 19 Alzheimer's disease (AD), and 17 normal cognitive (NC) subjects. Early- and late-phase BF-227 PET images were obtained 0–10 and 40–60 min after the injection, respectively. AS for late-phase BF-227 images were performed by 2 methods: (1) method A, for AS of late-phase BF-227 images using ^{8}F-fluorodeoxyglucose (FDG) images of the same subject and (2) method B, for AS of late-phase BF-227 images using early phase BF-227 images.
Results Method B was successfully used for AS in all cases. The Z score maps of 3D-SSP analyses of FDG PET and early phase BF-227 PET for AD and MCI groups showed a typical AD-like pattern. Regional analyses revealed that the early phase BF-227 PET showed significant differences between AD and NC, and MCI and NC.
Conclusion The early phase BF-227 PET images showed significant abnormal findings for the AD and MCI groups. AS of late-phase BF-227 images using early phase BF-227 images were successful, and enabled appropriate 3D-SSP analyses.

Keywords Amyloid imaging · Early phase · BF-227 · Alzheimer's disease · 3D-SSP

T. Kaneta (✉) · A. Arai · K. Takanami · S. Takahashi
Department of Diagnostic Radiology, Tohoku University, 1-1 Seiryomachi, Aobaku, Sendai 980-8574, Japan
e-mail: kaneta@rad.med.tohoku.ac.jp

N. Okamura · K. Yanai
Department of Pharmacology, Tohoku University Graduate School of Medicine, 4-1 Seiryomachi, Aobaku, Sendai 980-8575, Japan

K. Furukawa
Division of Brain Sciences, Department of Geriatrics and Gerontology, Institute of Development, Aging and Cancer, Tohoku University, 4-1 Seiryomachi, Aobaku, Sendai 980-8498, Japan

M. Tashiro · H. Arai
Division of Cyclotron Nuclear Medicine, Cyclotron and Radioisotope Center, Tohoku University, 6-3 Aoba, Aramaki, Aoba-ku, Sendai, Miyagi 980-8578, Japan

S. Furumoto · R. Iwata
Division of Radiopharmaceutical Chemistry, Cyclotron and Radioisotope Center, Tohoku University, 6-3 Aoba, Aramaki, Aoba-ku, Sendai, Miyagi 980-8578, Japan

Y. Kudo
Department of NeuroImaging Research, Innovation New Biomedical Engineering Center, Tohoku University, 4-1 Seiryomachi, Aobaku, Sendai 980-8498, Japan

Introduction

Three-dimensional stereotactic surface projection (3D-SSP) analysis [1, 2] has been widely used in voxel-based statistical analyses of ^{18}F-fluorodeoxyglucose (FDG) positron emission tomography (PET) and brain perfusion single-photon emission computed tomography (SPECT) data. In 3D-SSP analyses, anatomical standardization (AS) is performed using a brain template created from FDG PET data (the FDG template) [2], even for analyses of brain perfusion SPECT. It has been thought that 3D-SSP is

unsusceptible to the tracer distribution because of the usage of both a template and landmarks. Thus, 3D-SSP does not necessarily require individual templates for each tracer [3]. However, in analyses of amyloid PET, 3D-SSP analyses can sometimes cause errors because of inadequate AS, which might be caused by the large differences in distribution between FDG and amyloid tracers. Thus, a modified method of 3D-SSP analysis for amyloid PET using FDG PET has been developed [4]. In this method, an FDG PET scan of the same subject was used to calculate the parameters for AS, and these parameters were subsequently used for the AS of an amyloid PET scan. Recently, a few researchers focused on early phase amyloid PET scans using ^{11}C-Pittsburgh compound B (PiB) [5] and ^{18}F-florbetapir [6], and reported that early phase amyloid PET was potentially useful in providing complementary perfusion- or FDG-like information. In this study, we examined the suitability of early phase amyloid PET using ^{11}C-labeled 2-(2-[2-dimethylaminothiazol-5-yl]ethenyl)-6-(2-[fluoro]ethoxy)benzoxazole (BF-227) [7–9] for (1) conferring additional diagnostic value by providing perfusion-like information and (2) obtaining the appropriate AS in 3D-SSP analyses.

Methods

For the present study, we recruited 20 subjects with amnestic mild cognitive impairment (MCI), 19 subjects with Alzheimer's disease (AD), and 17 normal cognitive (NC) subjects. The diagnosis of AD and MCI was made according to the National Institute of Neurological and Communicative Diseases and Stroke/Alzheimer's Disease and Related Disorders Association criteria. The demographic information of the subjects is shown in Table 1. In this study, the subjects were overlapped with the previous study [4]. The NC group was recruited from among volunteers, none of whom were prescribed centrally acting medication, had cognitive impairment, or had cerebrovascular lesions identified on MRI. The study protocol was approved by the Committee on Clinical Investigation at our institution. After receiving information about the study, written informed consent was obtained from all participants.

Table 1 Demographic detail of the subjects in this study

	N	Gender	Age	MMSE
AD	19	M/F = 5/14	73.7 ± 7.0	20.0 ± 3.5
MCI	20	M/F = 10/10	76.6 ± 4.7	25.5 ± 2.3
NC	17	M/F = 8/9	67.0 ± 4.1	29.9 ± 0.3

AD Alzheimer's disease, *MCI* mild cognitive impairment, *NC* normal cognitive subject

All subjects underwent PET with both FDG and BF-227 within 3 months. All patients were clinically stable between the visits. BF-227 and its *N*-demethylated derivative (a precursor of BF-227) were custom-synthesized by Tanabe R&D Service Co., Japan. BF-227 was synthesized from its precursor by *N*-methylation in dimethyl sulfoxide using [^{11}C]methyl triflate. Both FDG and BF-227 PET were performed using a PET SET-2400W scanner (Shimadzu Inc., Japan) with a spatial resolution of 4 mm (transaxial) and 4.5 mm (axial) at full-width half-maximum (FWHM) in the center of the field of view. For attenuation correction, a transmission scan was performed using ^{68}Ge/Ga sources for 7 min. After intravenous bolus injection of 211–366 MBq of BF-227 (a volume of 2 cc) dynamic PET data were obtained for 60 min (23 sequential scans: 5 scans × 30 s, 5 scans × 60 s, 5 scans × 150 s, and 8 scans × 300 s) with each subject's eyes closed. The subject's head was fixed with a band. Head motion was monitored with a camera and an alarm. The data obtained 0–10 and 40–60 min after injection were used as early- and late-phase BF-227 PET data, respectively. For FDG PET, subjects were scanned in a quiet and dimly lit room with their eyes closed after fasting for at least 4 h. An emission scan of 15 min was started 45 min after an intravenous injection of approximately 370 MBq of FDG. The emission data were corrected for tissue attenuation based on the transmission data. These data were used for the calculation of standardized uptake value (SUV), a tissue radioactivity concentration normalized by injected dose and body weight.

Anatomical standardization of BF-227 images

Two kinds of AS for late-phase BF-227 images were performed: (1) method A, for AS of late-phase BF-227 images using FDG images of the same subject and (2) method B, for AS of late-phase BF-227 images using early phase BF-227 images. The specific procedures are described below. First, the FDG images and early phase BF-227 images were subjected to AS using an FDG template. Late-phase BF-227 images were then registered to the FDG images (method A) and to early phase BF-227 images (method B). AS was performed using transformation parameters calculated for the AS of the corresponding FDG images (method A) and for the early phase BF-227 images (method B). We used the software library Neurostat (University of Washington, Seattle, WA, USA) for neurological and biomedical image analyses. The precise programming methods have been described in [4]. The distortion of images after anatomical standardization was evaluated by reference to sample images with mild and severe distortion in [4].

Analysis

For voxel-based comparisons with normal subjects, normal databases were created by averaging the images from the NC group after AS by methods A and B, individually. The 3D-SSP Z-score map images were normalized to those of the cerebellum for late BF-227 images and to those of the pons for early BF-227 images and FDG images, and were shown to be within a range of 1–5 of the Z-score.

For voxel-based two-sample comparisons, a *t*-test was applied. Z-scores were calculated using the "ssp2tz" program in Neurostat. The 3D-SSP Z-map images were shown to be within a range of 1–5 of the Z-score.

Regional SUV values were extracted from cortical gray matter to the surface of the template by the 3D-SSP method, and were normalized by the value from the pons (nSUV). The values were calculated for the frontal, parietal, temporal, occipital and posterior cingulated cortices (PCC) using the "sspvoiclassic" program in Neurostat. The right and left lobes of each subject were analyzed evenly. For multiple comparisons between the 3 groups, we applied a Tukey-Kramer test using JMP Pro 9 (SAS Institute, NC, USA). For comparisons between the results from method A and B, we applied a paired *t*-test using Excel (Microsoft, WA, USA). Statistical significance was defined as $p < 0.05$.

Results

Comparison of FDG and early phase BF-227 PET

Case presentation

A 75-year-old man diagnosed with AD scored 19 on the mini-mental state examination (MMSE). As seen in Fig. 1, cross-sectional images and 3D-SSP results from FDG PET showed a typical AD-like pattern, which was characterized by decreased uptake in the PCC and parietal lobes. On the other hand, the cross-sectional images and 3D-SSP results of early phase BF-227 PET also showed a typical AD-like pattern, but the findings were less clear than those from FDG PET.

Group comparisons of FDG PET and early phase BF-227 PET

Figure 2 shows the Z-score maps from 3D-SSP analyses of FDG PET and early phase BF-227 PET, comparing the AD and NC groups and the MCI and NC groups. In both comparisons, FDG PET showed a typical AD-like pattern, which was characterized by decreased uptake in the PCC, parietal lobes, frontal lobes, and temporal lobes, but sparing the primary sensorimotor areas. Early phase BF-227 PET also showed a similar pattern, but the Z-scores were slightly lower than those from FDG PET.

Regional analyses

The regional analyses revealed that the mean nSUV values of FDG PET for the AD, MCI, and NC groups were in the ranges of 1.09–1.28, 1.14–1.27, and 1.28–1.42, respectively, whereas those of early phase BF-227 PET were found to be in the ranges of 0.93–1.06, 0.96–1.06, and 1.02–1.17, respectively. FDG PET showed significant differences between the AD and NC groups and between the MCI and NC groups in the parietal, temporal, and frontal lobes, and in the PCC (Fig. 3a). Early phase BF-227 PET also showed significant differences between them, with the exception of comparisons between the MCI and NC groups at the temporal lobes (Fig. 3b).

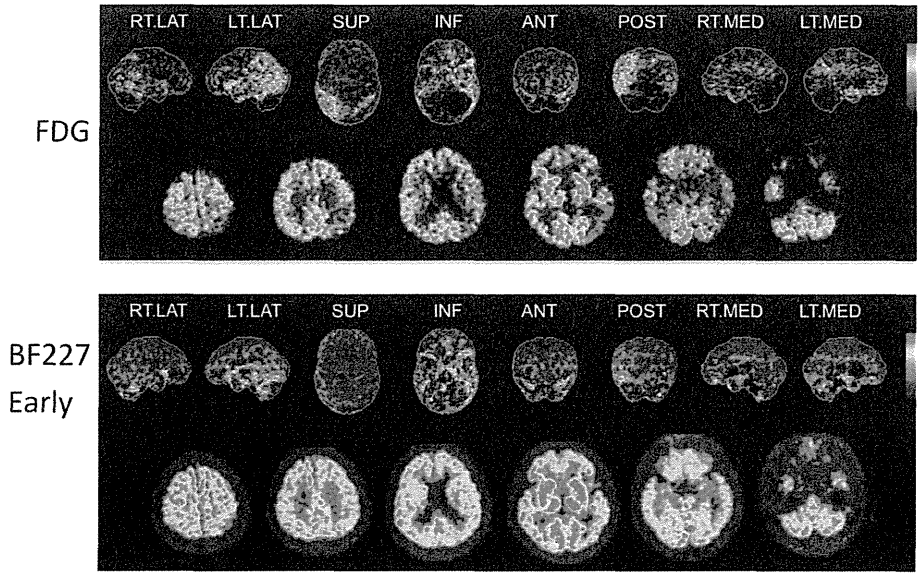

Fig. 1 Images of a 75-year-old man with AD. The mini-mental state examination (MMSE) score was 19. *Upper row* 3D-SSP results and cross-sectional images of FDG PET. *Lower row* 3D-SSP results and cross-sectional images of early phase BF-227 PET

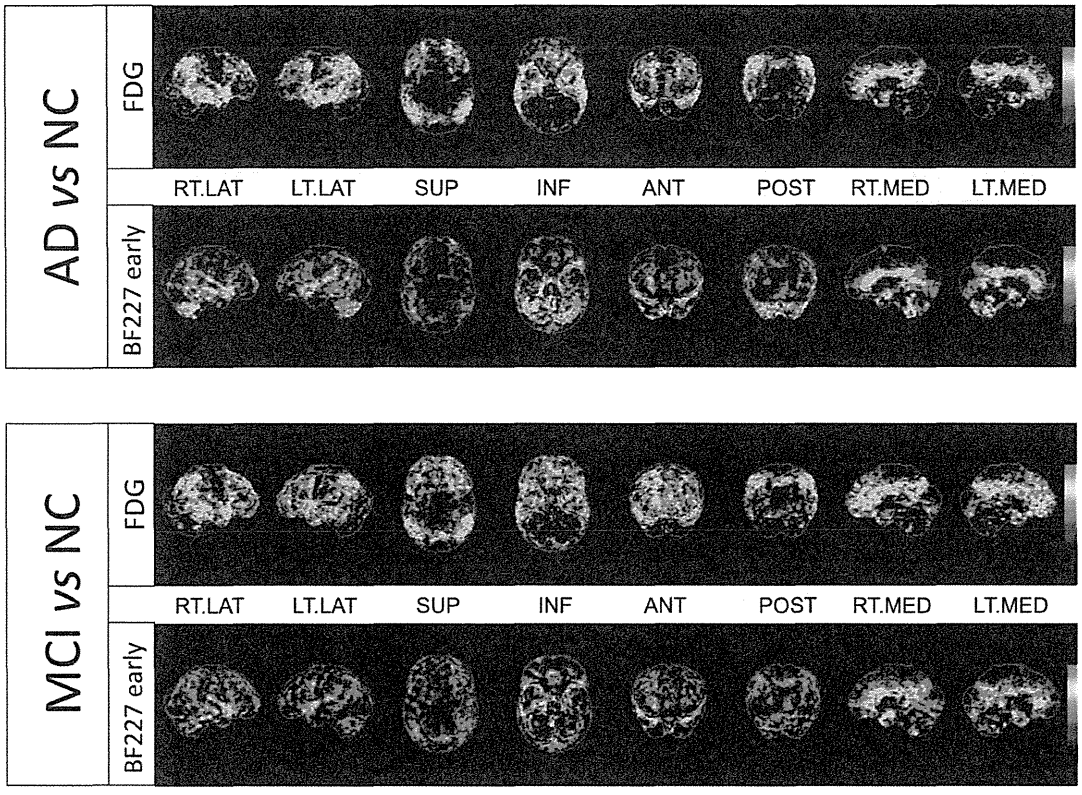

Fig. 2 Z score maps of 3D-SSP analyses of FDG PET and early phase BF-227 PET, comparing AD and NC groups (*upper*) and MCI and NC groups (*lower*)

Changes after anatomical standardization of late-phase BF-227 images

As reported previously [4], method A ("method 2" in the previous paper) was successfully used to perform AS in all but 2 cases. These 2 cases included 1 involving scan failure and another with an error in the registration of the BF-227 image to the FDG image; this necessitated their exclusion from subsequent analyses.

On the other hand, method B, which is a newly modified method using early phase BF-227 PET, was successfully used to perform AS in all cases.

Figure 4 shows sample images after AS from a 60-year-old female NC subject. Figure 4a–c demonstrate the images after AS using late-phase BF-227 images, method A, and method B, respectively. Figure 4a shows obvious distortion, especially in the frontal lobes, but Fig. 4b and c show successful AS.

Comparisons of the late-phase BF-227 images analyzed by methods A and B

Figure 5 shows the Z-score maps of late-phase BF-227 images after the 3D-SSP analyses using methods A and B, comparing the AD and NC groups and the MCI and NC groups. A comparison of the AD and NC groups using methods A and B showed almost the same distribution and values in the Z-score maps. A comparison of the MCI and NC groups using methods A and B showed almost the same distribution, but method B resulted in slightly lower values than method A. Table 2 shows the differences of nSUV derived from method A and B at the parietal, frontal, temporal and occipital lobe. There were no significant differences at the parietal, frontal and occipital lobe. But, there was a significant difference at the temporal lobe ($p < 0.01$).

Discussion

Early phase BF-227 images obtained in our study were totally different from late-phase images and more perfusion-like, and were compatible with those obtained in previous studies using PiB [5] and ^{18}F-florbetapir [6]. These amyloid PET tracers are highly lipophilic, and possibly have a higher first-pass influx rate (K_1) [10]. Thus, images obtained during early timeframes contain information related to K_1 [11]. These values of K_1 have also

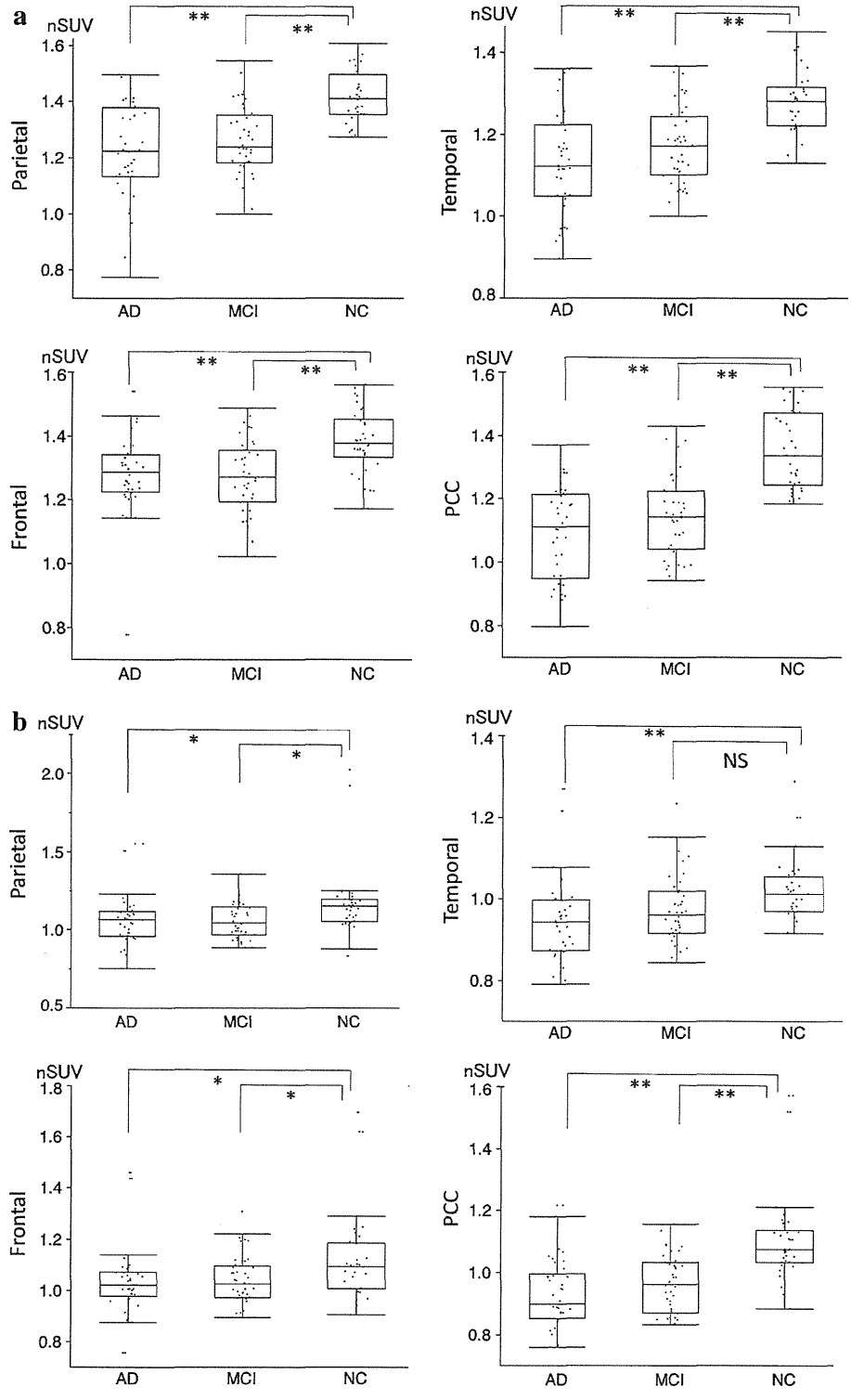

Fig. 3 Regional analyses of FDG PET (**a**) and early phase BF-227 PET (**b**) among AD, MCI, and NC groups. The values normalized to the pons were evaluated at the parietal, temporal, and frontal lobes and the posterior cingulated cortices (PCC). The box and whisker plots represent median (*horizontal line*), 1st quartile (*lower limit of box*), 3rd quartile (*upper limit of box*), and minimum and maximum values, respectively. $^{**}p < 0.01$, $^{*}p < 0.05$, *NS* not significant

been found to represent unidirectional influx of the tracer into the brain and are related to perfusion [12]. In addition, correlations between metabolism and cerebral perfusion have been long established in healthy older individuals and in those with degenerative dementias, likely because reduced metabolic demand is related to reduced perfusion [13]. Thus, it is not surprising that early PET frames of amyloid tracers show perfusion-like or FDG-like images.

Hereinafter, we discuss the benefits of obtaining these images.

Our results showed that the appropriate AS of 3D-SSP was successfully performed using early phase BF-227 images. Previously, we used FDG images for the AS of 3D-SSP because 3D-SSP uses an FDG template [1, 2]. The images obtained from early phase BF-227 PET were successfully transformed to the FDG template during the AS of 3D-SSP. Our modified 3D-SSP methods rely on the accurate co-registration of the images of the same subject using linear transformations, such as rotation, stretching, shrinking, and shearing. Non-linear warping is not necessary for the co-registration of images from the same subject. Thus, the co-registration of FDG and BF-227 images, or that of early- and late-phase BF-227 images can be performed accurately. However, method A produced an error in the registration of the BF-227 image to the FDG image in 1 case, while method B did not produce any errors. This can be explained by the smaller degree of dislocation between early- and late-phase BF-227 scans than between the FDG and BF-227 scans. Early- and late-phase BF-227 scans were performed on the same day without repositioning the patients' bodies, whereas

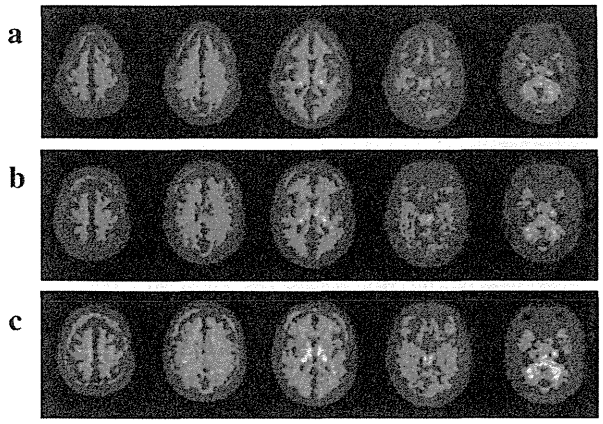

Fig. 4 Sample images after AS of 60-year-old female NC subject. **a–c** demonstrate the images after AS using late-phase BF-227 images, method A, and method B, respectively

Table 2 Comparison of nSUV between the results of methods A and B

	Parietal	Temporal*	Frontal	Occipital
Method A	1.03 ± 0.01	1.06 ± 0.01	1.05 ± 0.01	1.07 ± 0.01
Method B	1.02 ± 0.01	1.04 ± 0.01	1.03 ± 0.01	1.07 ± 0.01

* $p < 0.01$

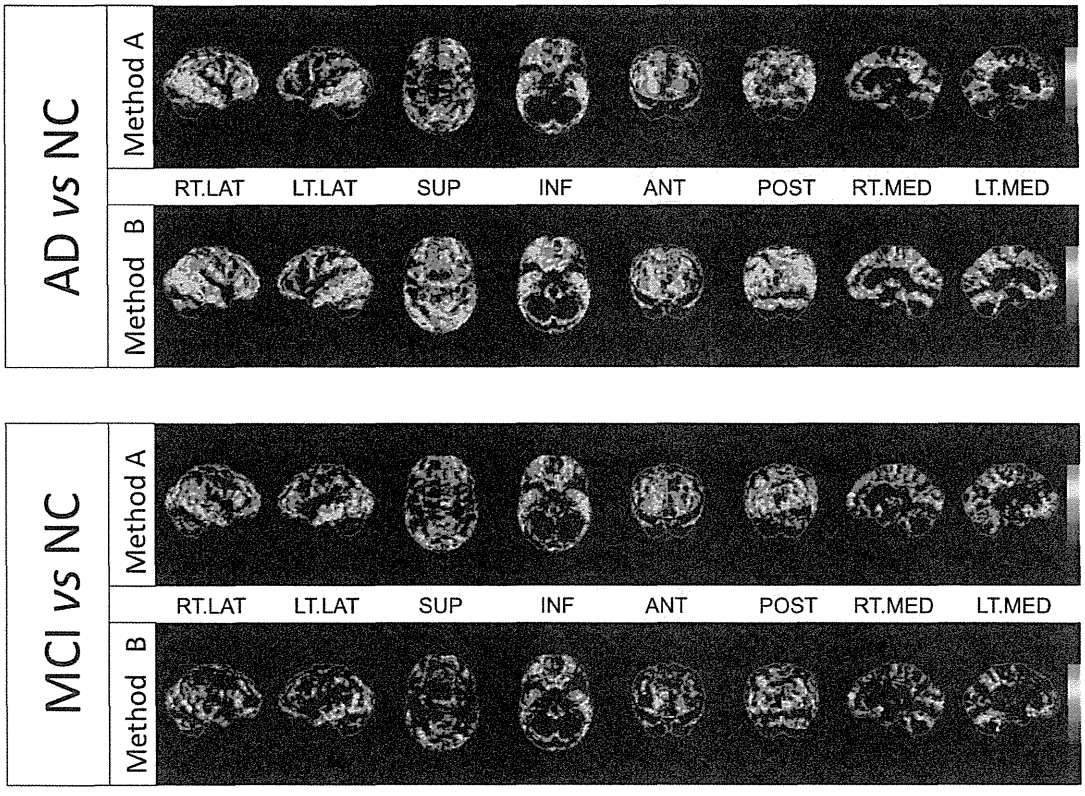

Fig. 5 Z score maps of late-phase BF-227 images after 3D-SSP analyses comparing AD and NC groups (*upper*) and MCI and NC groups (*lower*) by methods A and B

the FDG and BF-227 scans were performed with an interval between of several days to a few months. Thus, it may be preferable to use method B to obtain an appropriate AS. In addition, FDG images may not necessarily be required for the 3D-SSP analysis of amyloid PET. This could reduce the need for an additional patient visit or higher exposure to the radioactivity of FDG imaging. Furthermore, no significant differences were observed between the results of 3D-SSP performed by methods A and B. As shown in Fig. 5, no significant differences were found between methods A and B in the AD group versus the NC group. For the MCI group versus the NC group, the abnormal findings obtained with method B appear slightly smaller in the Z-score maps than those obtained with method A. Table 2 showed a significant difference in nSUV derived from methods A and B at the temporal lobe only, but not at the parietal, frontal and occipital lobes. The reason for such differences remains unknown. However, it might be caused by the difference of the tracer distribution around the temporal lobe between FDG and early phase BF-227, or the sampling method of "sspvoiclassic" in Neurostat.

Next, our results showed that early phase BF-227 images were significantly different between the AD and NC groups and between the MCI and NC groups in the parietal, temporal, and frontal lobes, and in the posterior cingulate cortices in all cases, except between the MCI and NC groups in the temporal lobes. These results are similar to those obtained with the FDG images, and suggest that early phase BF-227 images have equivalent diagnostic power to FDG images in terms of group comparisons between AD and NC, and MCI and NC. However, the visual evaluation of early phase BF-227 images may be still difficult for individual diagnosis. As shown in Figs. 1 and 2, the FDG PET findings were clearer than those from early phase BF-227 PET. One of the main reasons might be the lack of optimization of early phase scanning time. From the results of time activity curves of BF-227 [8], AD patients showed a significant difference over 10 min in the cortical areas and cerebellum, but normal subjects showed no significant differences. Thus, we set the early phase as a timeframe of 0–10 min, which seemed not to be amyloid-specific, but rather perfusion-like. However, optimization of scanning time may improve the image quality and the adherence to perfusion or FDG images. In previous studies that compared various time frames, scanning times of 1–8 min for PiB [5] and 1–6 min for AV-45 [6] were thought to be optimal for early phase imaging. As another limitation of this study, significant differences in age were seen between AD and NC, and MCI and NC groups. This study mainly focused on the methodological aspect, however, age-matched NC subjects should be compared in the clinical setting.

In conclusion, early phase BF-227 images were perfusion-like, and showed significant differences between the AD and NC groups, and between the MCI and NC groups. In addition, we developed a modified method for 3D-SSP analyses using early phase BF-227 PET. The results of this study demonstrate that the use of early phase images may improve the utility of amyloid PET for further dementia studies.

Acknowledgments This work was supported by JSPS KAKENHI Grant Number 24591745.

Conflict of interest The authors declare that they have no conflict of interest.

References

1. Minoshima S, Koeppe RA, Frey KA, Kuhl DE. Anatomic standardization: linear scaling and nonlinear warping of functional brain images. J Nucl Med. 1994;35:1528–37.
2. Minoshima S, Frey KA, Koeppe RA, Foster NL, Kuhl DE. A diagnostic approach in Alzheimer's disease using three-dimensional stereotactic surface projections of fluorine-18-FDG PET. J Nucl Med. 1995;36:1238–48.
3. Yamamoto Y, Onoguchi M. Statistical image analysis method to use for cerebral blood flow SPECT examination: difference and matters that require attention of processing of eZIS and iSSP. Nihon Hoshasen Gijutsu Gakkai Zasshi. 2011;67:718–27 (Japanese).
4. Kaneta T, Okamura N, Minoshima S, Furukawa K, Tashiro M, Furumoto S, et al. A modified method of 3D-SSP analysis for amyloid PET imaging using [^{11}C]BF-227. Ann Nucl Med. 2011;25:732–9.
5. Rostomian AH, Madison C, Rabinovici GD, Jagust WJ. Early 11C-PIB frames and 18F-FDG PET measures are comparable: a study validated in a cohort of AD and FTLD patients. J Nucl Med. 2011;52:173–9.
6. Hsiao IT, Huang CC, Hsieh CJ, Hsu WC, Wey SP, Yen TC, et al. Correlation of early-phase 18F-florbetapir (AV-45/Amyvid) PET images to FDG images: preliminary studies. Eur J Nucl Med Mol Imaging. 2012;39:613–20.
7. Kudo Y. Development of amyloid imaging PET probes for an early diagnosis of Alzheimer's disease. Minim Invasive Ther Allied Technol. 2006;15:209–13.
8. Kudo Y, Okamura N, Furumoto S, Tashiro M, Furukawa K, Maruyama M, et al. 2-(2-[2-Dimethylaminothiazol-5-yl]ethenyl)-6-(2-[fluoro]ethoxy)benzoxazole: a novel PET agent for in vivo detection of dense amyloid plaques in Alzheimer's disease patients. J Nucl Med. 2007;48:553–61.
9. Furumoto S, Okamura N, Iwata R, Yanai K, Arai H, Kudo Y. Recent advances in the development of amyloid imaging agents. Curr Top Med Chem. 2007;7:1773–89.
10. Treyer V, Streffer J, Wyss MT, Bettio A, Ametamey SM, Fischer U, et al. Evaluation of the metabotropic glutamate receptor subtype 5 using PET and 11C-ABP688: assessment of methods. J Nucl Med. 2007;48:1207–15.
11. Koeppe RA, Gilman S, Joshi A, Liu S, Little R, Junck L, et al. 11C-DTBZ and 18F-FDG PET measures in differentiating dementias. J Nucl Med. 2005;46:936–44.
12. Blomquist G, Engler H, Nordberg A, Ringheim A, Wall A, Forsberg A, et al. Unidirectional influx and net accumulation of PIB. Open Neuroimaging J. 2008;2:114–25.
13. Silverman DH. Brain ^{18}F-FDG PET in the diagnosis of neurodegenerative dementias: comparison with perfusion SPECT and with clinical evaluations lacking nuclear imaging. J Nucl Med. 2004;45:594–607.

Novel ^{18}F-Labeled Arylquinoline Derivatives for Noninvasive Imaging of Tau Pathology in Alzheimer Disease

Nobuyuki Okamura[1], Shozo Furumoto[1,2], Ryuichi Harada[1], Tetsuro Tago[2], Takeo Yoshikawa[1], Michelle Fodero-Tavoletti[3], Rachel S. Mulligan[4], Victor L. Villemagne[4], Hiroyasu Akatsu[5], Takayuki Yamamoto[5], Hiroyuki Arai[6], Ren Iwata[2], Kazuhiko Yanai[1], and Yukitsuka Kudo[7]

[1]Department of Pharmacology, Tohoku University School of Medicine, Sendai, Japan; [2]Division of Radiopharmaceutical Chemistry, Cyclotron and Radioisotope Center, Tohoku University, Sendai, Japan; [3]Department of Pathology, University of Melbourne, Victoria, Australia; [4]Department of Nuclear Medicine and Centre for PET, Austin Health, Melbourne, Victoria, Australia; [5]Choju Medical Institute, Fukushimura Hospital, Toyohashi, Japan; [6]Department of Geriatrics and Gerontology, Institute of Development, Aging and Cancer, Tohoku University, Sendai, Japan; and [7]Clinical Research, Innovation and Education Center, Tohoku University Hospital, Sendai, Japan

Neurofibrillary tangles in Alzheimer disease (AD) brains are composed of the microtubule-associated protein tau. Noninvasive monitoring of tau protein aggregates in the living brain will provide useful information regarding tau pathophysiology in AD. However, no PET probes are currently available for selective detection of tau pathology in AD. We have previously reported ^{18}F-labeled THK-523 (^{18}F-6-(2-fluoroethoxy)-2-(4-aminophenyl)quinoline) as a tau imaging radiotracer candidate for PET. After compound optimization, we developed novel ^{18}F-labeled arylquinoline derivatives, ^{18}F-THK-5105 and ^{18}F-THK-5117, for use as tau imaging PET tracers. **Methods:** ^{18}F-labeled compounds were prepared from the corresponding tosylated precursors. The binding affinity of compounds to synthetic tau aggregates and tau-rich AD brain homogenates was determined by saturation and competition binding assays. The binding selectivity of compounds to tau pathology was evaluated by autoradiography of AD brain sections. The pharmacokinetics of compounds were assessed in biodistribution studies in normal mice. A 14-d toxicity study with intravenous administration of compounds was performed using rats and mice. **Results:** In vitro binding assays demonstrated higher binding affinity of THK-5105 and THK-5117 than THK-523 to tau protein aggregates and tau-rich AD brain homogenates. Autoradiographic analyses of AD brain sections showed that these radiotracers preferentially bound to neurofibrillary tangles and neuropil threads, which colocalized with Gallyas-positive and immunoreactive tau protein deposits. The distribution of this radiotracer binding in AD brain sections was completely different from that of ^{11}C-Pittsburgh compound B, showing preferential binding to amyloid plaques. Furthermore, these derivatives demonstrated abundant initial brain uptake and faster clearance in normal mice than ^{18}F-THK-523 and other reported ^{18}F-labeled radiotracers. THK-5105 and THK-5117 showed no toxic effects related to the administration of these compounds in mice and rats and no significant binding for various neuroreceptors, ion channels, and transporters at 1-μM concentrations. **Conclusion:** ^{18}F-labeled THK-5105 and THK-5117 are promising candidates as PET tau imaging radiotracers.

Received Nov. 19, 2012; revision accepted Feb. 19, 2013.
For correspondence or reprints contact: Nobuyuki Okamura, 2-1, Seiryo-machi, Aoba-ku, Sendai 980-8575 Japan.
E-mail: nookamura@med.tohoku.ac.jp
Published online Jul. 15, 2013.

Key Words: Alzheimer disease; tau; neurofibrillary tangles; positron emission tomography; molecular imaging

J Nucl Med 2013; 54:1420–1427
DOI: 10.2967/jnumed.112.117341

Alzheimer disease (AD) is the most common cause of dementia in the elderly. At present, approximately 18 million people worldwide have AD, and this number is estimated to double by 2025 (*1*). The major pathologic hallmarks of AD are senile plaques (SPs) and neurofibrillary tangles (NFTs). SPs are composed of amyloid-β protein (Aβ), a 39–43 amino acid protein product derived from the proteolytic cleavage of the amyloid precursor protein. Abnormalities in the production or clearance of Aβ are considered to be the initiating events in AD pathogenesis (*2*). Excessive Aβ concentrations lead to its aggregation and formation of SPs, followed by NFT formations, synaptic dysfunction, and neuronal death. NFTs are composed of hyperphosphorylated tau, a microtubule-associated protein that stabilizes microtubule assembly in axons (*3*). Tau accumulation is also recognized as neuropil threads and dystrophic neurites in the AD brain (*4*). Phosphorylation of tau decreases its ability to bind to microtubules, which are destabilized, leading to neuronal death. NFT lesions follow a stereotypical pattern, initially appearing in the transentorhinal cortex, followed by the entorhinal cortex and the hippocampus, and subsequently the neocortex (*5*). In AD patients, the severity of tau pathology is closely related to neuronal loss (*6,7*) and cognitive impairment (*8,9*). The deposition of NFTs is thought to begin before extensive neuronal loss and cognitive decline occur. Thus, noninvasive detection of tau pathology would be useful to predict future cognitive decline in the preclinical stages of AD and to track disease progression before extensive neuronal loss occurs.

Several researchers have focused on developing radiotracers for imaging tau pathology in the human brain (*10–17*). Tau imaging radiotracers need to cross the blood–brain barrier and to have a high binding affinity to NFTs with minimal nonspecific binding (*18*). 2-(1-(6-[(2-^{18}F-fluoroethyl)(methyl)amino]-2-naphthyl)ethylidene)malononitrile (^{18}F-FDDNP) is claimed as the only PET tracer that allows measurement of the amount of tau protein

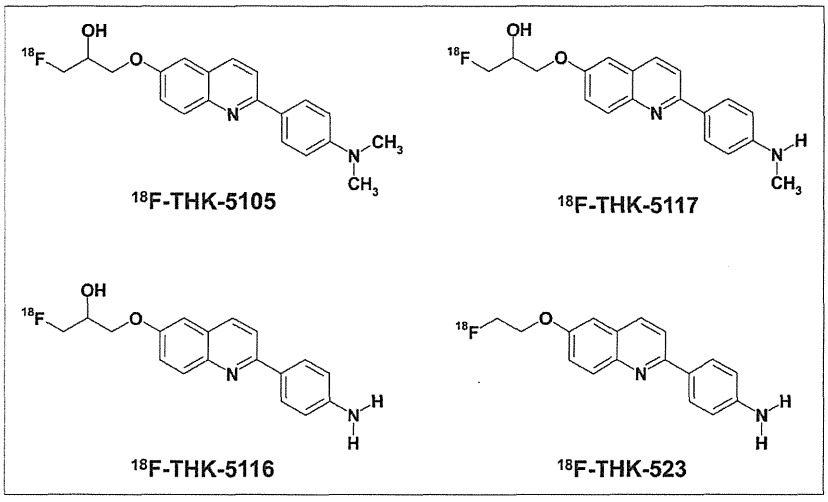

FIGURE 1. Chemical structures of ^{18}F-THK-5105, ^{18}F-THK-5116, ^{18}F-THK-5117, and ^{18}F-THK-523.

deposits in the human brain (*19*). However, ^{18}F-FDDNP was found to have lower binding affinity for protein fibrils than ^{11}C-Pittsburgh compound B (^{11}C-PiB) (*20,21*). In addition, this tracer has been claimed to bind to both SPs and NFTs equally (*22*). In the neocortex of the AD brain, SPs and NFTs colocalize with each other, where Aβ concentrations are 5–20 times higher than that of tau (*23,24*). In such cases, the signal from the SPs would be so overwhelming that it would obscure the signal from the NFTs. Therefore, the development of selective tau imaging tracers is necessary for accurate and quantitative evaluation of tau pathology in AD.

In the past few years, we also have screened more than 2,000 compounds to develop novel radiotracers with high affinity and selectivity for tau aggregates. Consequently, we identified a series of novel quinoline and benzimidazole derivatives that bind NFTs and, to a lesser extent, Aβ plaques (*10*). Serial analyses of these compounds led to the design and synthesis of the novel tau imaging agent ^{18}F-6-(2-fluoroethoxy)-2-(4-aminophenyl)quinoline (^{18}F-THK-523) (*15,17*). Preclinical analyses of ^{18}F-THK-523 indicated that this tracer selectively labels tau pathology in the AD brain. However, the preclinical data suggest that the pharmacokinetics and binding characteristics of ^{18}F-THK-523 might not reach the necessary optimal levels required for PET tracers. Through our optimization process, we developed novel ^{18}F-labeled 2-arylquinoline derivatives that are promising candidates for in vivo tau imaging probes. In this study, we performed the preclinical evaluation of the binding and pharmacokinetic properties of these compounds.

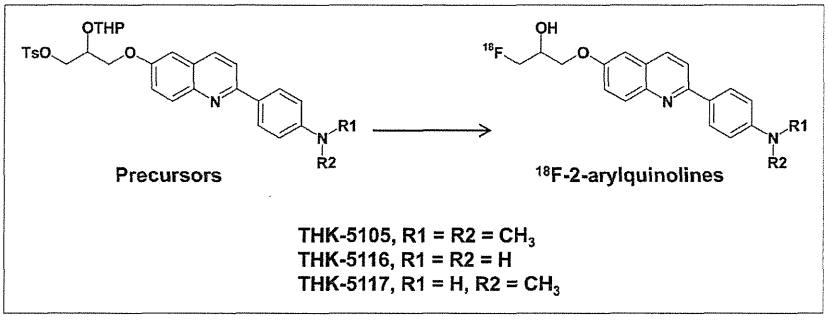

FIGURE 2. Radiosynthesis scheme of ^{18}F-2-arylquinolines.

MATERIALS AND METHODS

Synthesis and Radiosynthesis of 2-Arylquinoline Derivatives

The chemical structures of 6-[(3-^{18}F-fluoro-2-hydroxy)propoxy]-2-(4-dimethylaminophenyl)quinoline (^{18}F-THK-5105), 6-[(3-^{18}F-fluoro-2-hydroxy)propoxy]-2-(4-methylaminophenyl)quinoline (^{18}F-THK-5117), 6-[(3-^{18}F-fluoro-2-hydroxy)propoxy]-2-(4-aminophenyl)quinoline (^{18}F-THK-5116), and ^{18}F-THK-523 are shown in Figure 1. ^{18}F-THK-5105, ^{18}F-THK-5116, and ^{18}F-THK-5117 were prepared from the corresponding tosylate precursors according to the scheme as indicated in the Figure 2. Details on their syntheses will be described elsewhere (S. Furumoto et al., unpublished data, 2013). Briefly, the aqueous ^{18}F$^-$ contained in the K_2CO_3 solution (1.59–3.69 GBq) and Kryptofix222 (15 mg) were placed in a brown vial. Water was removed by azeotropic evaporation with acetonitrile. After being dried, the activated ^{18}F-KF/Kryptofix222 was reacted with the precursor (3 mg) in dimethylsulfoxide (0.7 mL) at 110°C for 10 min. Then, 2 M HCl was added to the solution, followed by an additional 3-min reaction for deprotection of the hydroxyl group. After neutralization with 4 M AcOK, the product was purified by semipreparative high-performance liquid chromatography (HPLC) (column: Inertsil ODS-4 [GL Sciences, Inc.]; mobile phase: 20 mM NaH_2PO_4/acetonitrile [55/45 for THK-5105 and THK-5117, 65/35 for THK-5116]; flow rate: 5.0 mL/min). The radiolabeled product was dissolved in ethanol, dimethylsulfoxide, or saline with polysobate-80 (<0.1%) for biologic evaluation.

^{18}F-THK-523 and ^{18}F-FDDNP were also prepared in a manner similar to the one described above using the corresponding tosylate precursors reported previously (*15,25,26*). ^{11}C-PiB was radiolabeled using its precursor (2-(4-aminophenyl)-6-methoxymethoxybenzothiazole) and ^{11}C-methyl triflate, as previously described (*27*).

Determination of Log P Values

Log P values were determined by the HPLC method according to the guideline of the Organisation for Economic Co-operation and Development (OECD Guideline for Testing of Chemicals: Partition Coefficient (n-octanol/water), High Performance Liquid Chromatography [HPLC] Method), with slight modification. Briefly, 12 reference compounds whose log P values ranged between 0.5 and 4.0 were analyzed by HPLC under the following conditions: HPLC, a JASCO LC-2000 Plus series (JASCO); column, Inertsil ODS-4 (4.6 × 150 mm, 5 μm; GL Sciences, Inc.); mobile phase, 20 mM NaH_2PO_4 (pH 7.4)/acetonitrile (55/45); flow rate, 1.5 mL/min; ultraviolet absorbance, 245 nm; and column temperature, 40°C. Then, a calibration curve of log (tR − t0) (tR, retention time; t0, dead time) versus log P of each reference compound was created (R^2 = 0.9469). Test compounds listed in Table 1 were also analyzed by the same HPLC method to measure log (tR − t0) values that were used for determination of log P values from the calibration curve.

In Vitro Binding Assays

Synthetic human Aβ1–42 was purchased from Peptide Institute Inc. Recombinant K18ΔK280-tau protein was obtained from Life Technologies Japan Ltd. Fibrils of

TABLE 1
Log P and Brain Uptake After Intravenous Administration of ^{18}F-Labeled Compounds in Mice

Compound	Log P	Brain uptake (%ID/g) 2 min after injection	30 min after injection	60 min after injection	Brain uptake ratio (2 min/60 min)
^{18}F-THK-523	2.40	2.72	1.47	1.46	1.86
^{18}F-THK-5105	3.03	9.20	3.61	1.00	9.20
^{18}F-THK-5116	1.57	3.36	0.75	0.57	5.89
^{18}F-THK-5117	2.32	6.06	0.59	0.26	23.1
^{18}F-FDDNP	3.71	6.23	2.02	2.14	2.91

Aβ1–42 and K18ΔK280-tau were prepared as described previously (*15*). Briefly, synthetic Aβ1–42 (200 μM) and K18Δ280K-tau (20 μM) solutions in phosphate-buffered saline (PBS) were incubated at 37° C with agitation for 3–4 d. We additionally prepared AD brain homogenates for binding assay, because the structural conformation of synthetic protein fibrils does not fully correlate with the structure of native protein deposits in the human brain. Human brain tissue was isolated from a mesial temporal frozen sample of an AD patient and homogenized in PBS. Brain tissue homogenate aliquots were taken and frozen at −80°C until used. Insoluble Aβ and tau levels were determined using a human β-amyloid enzyme-linked immunosorbent assay (ELISA) kit (Wako) and a human tau ELISA kit (Life Technologies Japan Ltd.), respectively. Next, brain homogenates and the solutions of synthetic Aβ1–42 or K18Δ280K-tau fibrils were incubated with increasing concentrations of ^{18}F-THK-5105 (0.1–250 nM). To account for nonspecific binding of ^{18}F-THK-5105, the reactions were performed in triplicate in the presence of 2 μM unlabeled THK-5105. The binding reactions were incubated for 1 h at room temperature in assay buffer (Dulbecco PBS; 0.1% bovine serum albumin). Bound radioactive compounds were separated from free radioactive compounds by filtration under reduced pressure (MultiScreen HTS Vacuum Manifold; Millipore). Filters were washed three times with assay buffer, and the radioactivity contained within the filters was counted in a γ-counter (AccuFLEX γ7000, Aloka, Tokyo, Japan). Binding data were analyzed using curve-fitting software that calculates the K_d and B_{max} (K_d is dissociation constant and B_{max} is maximum number of binding sites, respectively) using nonlinear regression (GraphPad Prism; GraphPad Software).

For inhibition studies, the assay buffer containing each compound (0.1–1,000 nM), ^{18}F-THK-5105 (1.76 nM, ~37 kBq), K18Δ280K-tau (200 nM), and 0.1% bovine serum albumin was incubated at room temperature for 1 h. Nonspecific binding was determined in the presence of 10 μM THK-5105. The mixture was filtered through Multiscreen HTS 96-well filtration plates, followed by washing three times with PBS (0.1% bovine serum albumin), and the filters containing bound ^{18}F ligand were counted in a γ-counter. The percentage of bound radioligand at each concentration was measured in triplicate and then plotted against the inhibitor concentration. Half-maximal inhibitory concentration values were determined from the displacement curves using the GraphPad Prism software. Inhibition constant (K_i) values were calculated from the half-maximal inhibitory concentration values using the Cheng–Prusoff equation (*28*).

TABLE 2
K_d and B_{max} Values of ^{18}F-THK-5105 for Synthetic Tau and $Aβ_{1–42}$ Fibrils

Protein	K_{d1}	B_{max1}	K_{d2}	B_{max2}
Tau	1.45	6.89	7.40	20.05
$Aβ_{1–42}$	35.9	61.6		

K_d are in nM and Bmax are in pmol ^{18}F-THK-5105/nmol fibrils.

Tissue Staining

Experiments were performed under the regulations of the ethics committee of Tohoku University School of Medicine. Paraffin-embedded hippocampal brain sections from an autopsy-confirmed AD case (78-y-old woman) were used for tissue staining with THK-5105. Brain sections were obtained from Fukushimura Hospital. After deparaffinization, autofluorescence quenching was performed as previously described (*29*). Quenched tissue sections were immersed for 10 min in a 100-μM THK-5105 solution containing 50% ethanol. Sections were then dipped briefly into water, rinsed in PBS, coverslipped with FluorSave Reagent (Calbiochem), and examined using an Eclipse microscope (Nikon) equipped with a blue-violet filter (excitation, 400–440 nm; dichroic mirror, 455 nm; barrier filter, 470 nm). Sections stained with THK-5105 were subsequently immunostained with the AT8 anti-tau antibody (diluted 1:20; Innogenetics). After incubation at 4°C in the primary antibody for 16 h, sections were processed by the avidin-biotin method using a Pathostain ABC-POD(M) Kit (Wako) and diaminobenzidine as a chromogen. Sections were additionally stained using a modified Gallyas–Braak method (pretreatment with 0.3% potassium permanganate for 10 min, followed by 0.1% oxalic acid for 3 min) (*30*).

Autoradiography of Human Brain Sections

For the autoradiographic study, 8-μm-thick paraffin-embedded brain sections from a healthy control (62-y-old man) and 2 AD patients (69-y-old man and 92-y-old woman) were used. After deparaffinization, sections were incubated for 10 min at room temperature with radiolabeled compounds (0.5 MBq/mL) and washed briefly with water and 50% ethanol. After being dried, the labeled sections were exposed overnight to a BAS-III imaging plate (Fuji Film). The autoradiographic images were obtained using a BAS-5000 phosphoimaging instrument (Fuji Film). The neighboring sections were stained

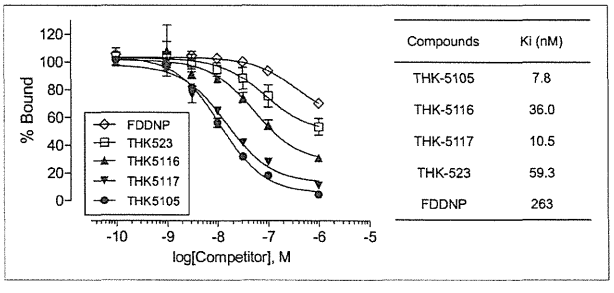

FIGURE 3. Competitive inhibition of ^{18}F-THK-5105 binding by 2-arylquinolines and FDDNP to tau protein fibrils. K_i values for inhibition of ^{18}F-THK-5105 binding to tau are shown.

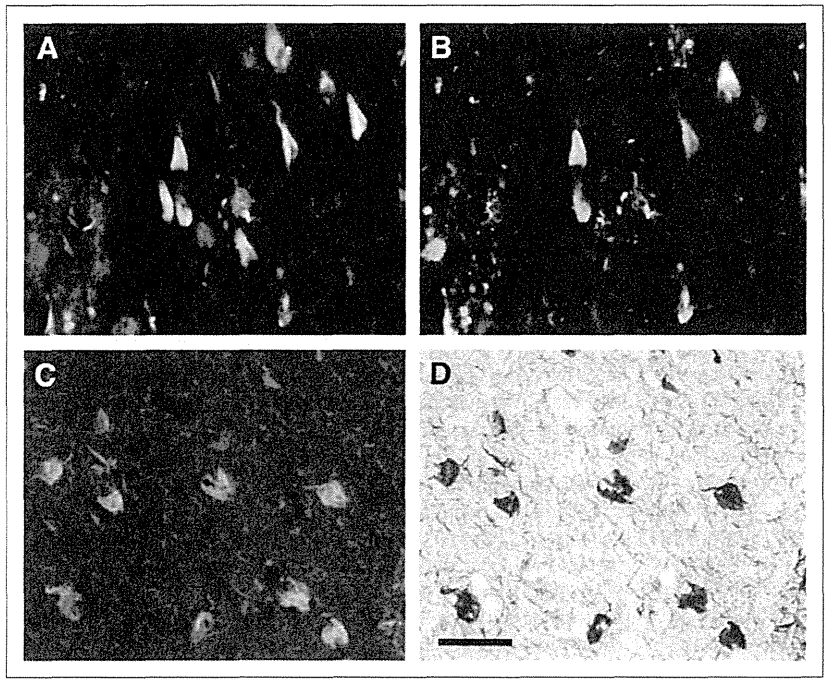

FIGURE 4. Neuropathologic staining of brain sections from AD patients. Neurofibrillary tangles and neuropil threads were clearly stained with THK-5105 (A and C). These stainings were consistent with tau immunostaining (B) and Gallyas–Braak staining (D) in same sections. Bar = 50 μm.

using a modified Gallyas–Braak method or immunostained using the AT8 anti-tau monoclonal antibody (diluted 1:20; Innogenetics), the 4G8 Aβ antibody (diluted 1:100; Signet), or the 6F/3D Aβ antibody (diluted 1:50; Dako). For correlational analysis of the autoradiographic and immunohistochemical images, 36 circular regions of interest (the area of each region of interest was ~7 mm^2) were placed on the gray matter of the hippocampus, parahippocampal gyrus, fusiform gyrus, temporal gyri (superior, middle, and inferior), insula, pre- and postcentral gyri, superior frontal gyrus, paracentral lobule, and cingulate gyrus. The percentage area of positive signals in each region of interest was calculated using ImageJ software (National Institutes of Health). A correlational analysis between percentage areas of tracer binding and positive immunostaining was performed using Pearson simple correlation.

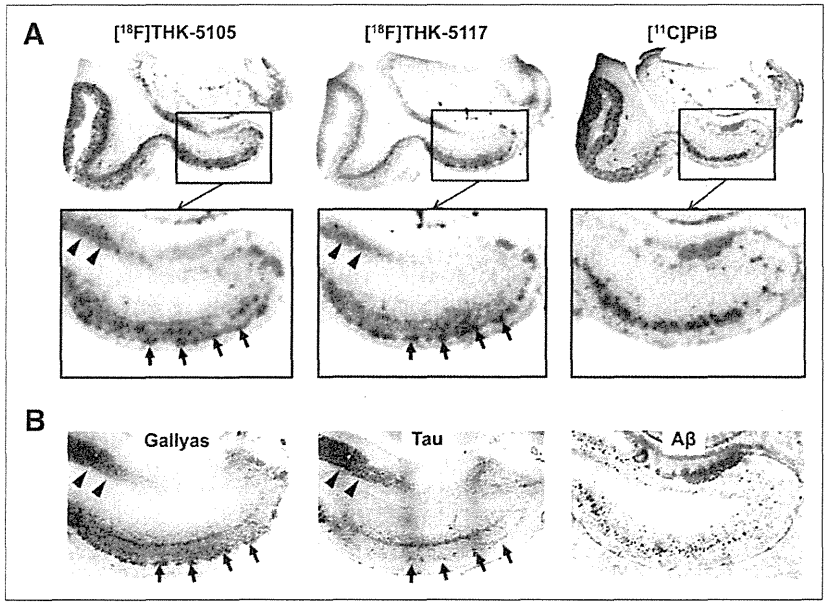

FIGURE 5. (A) Autoradiographic images of ^{18}F-THK-5105, ^{18}F-THK-5117, and ^{11}C-PiB binding in mesial temporal section from AD patient. (B) Gallyas–Braak silver staining (left) and immunostaining with anti-tau (center) and anti-Aβ (right) antibodies in adjacent brain sections. Arrowheads = CA1 area of hippocampus; longer arrows = entorhinal cortex.

Biodistribution in Mice

The experimental protocol of animal study was approved by the Ethics Committee of Tohoku University School of Medicine. ^{18}F-labeled tracers (1.1–6.3 MBq) were injected into the tail vein of male ICR mice (n = 20; mean weight, 28–32 g). Mice were then sacrificed by decapitation at 2, 10, 30, 60, and 120 min after injection. The brain, blood, liver, kidney, and femur were removed and weighed, and radioactivity was counted with an automatic γ-counter. The percentage injected dose per gram of tissue (%ID/g) was calculated by comparing tissue counts to tissue weight. Each %ID/g value is expressed as a mean ± SD of 4 separate experiments.

Animal Toxicity Studies

A 14-d toxicity study with intravenous administration of a single dose of THK-5105 and THK-5117 was performed using Sprague–Dawley rats and ICR mice. Briefly, the study included 3 groups of male and female rats and mice that were administered 0 (group 1), 0.1 (group 2), and 1 (group 3) mg/kg of test article (10% dimethylsulfoxide/90% distilled water) per rat or mouse by intravenous injection on study day 1. The study included clinical observations plus body weight measurements for a 14-d observation period. Hematology and pathologic examinations were conducted on study days 2 and 15. Detailed necropsies with external examinations were also performed.

Receptor Binding Assays

Receptor binding screens were conducted by Sekisui Medical Inc. Binding inhibition effects of 1 μM THK-5105 and THK-5117 were evaluated in competitive radioligand assays against 60 common neurotransmitter receptors, ion channels, and transporters. Percentage inhibition ratios were calculated by the following equation: inhibition ratio (%) = $[1 - (B - N)/(B_0 - N)] \times 100$, where N is the nonspecific bound radioactivity, and B and B_0 are the bound radioactivity in the presence and absence of tested compounds, respectively. Data are expressed as the mean values of duplicate samples.

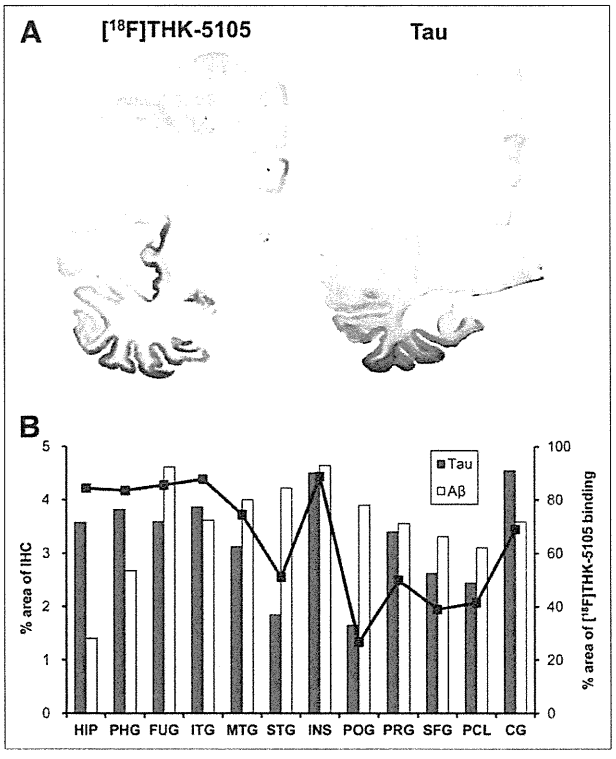

FIGURE 6. (A) Autoradiography of hemibrain sections from AD patient with ^{18}F-THK-5105 and tau immunostaining in neighboring section. (B) Region-of-interest analysis indicated that percentage areas of ^{18}F-THK-5105 binding (line plots) were significantly correlated with percentage areas of tau immunostaining (gray bars) but not with that of Aβ immunostaining (white bars). CG = cingulate gyrus; HIP = hippocampus; FUG = fusiform gyrus; IHC = immunohistochemistry; INS = insula; ITG = inferior temporal gyrus; MTG = middle temporal gyrus; PCL = paracentral lobule; PHG = parahippocampal gyrus; POG = postcentral gyrus; PRG = precentral gyrus; SFG = superior frontal gyrus; STG = superior temporal gyrus.

RESULTS

Radiosynthesis

All radiolabeled compounds were obtained in greater than 97% radiochemical purities after HPLC purification. The decay-corrected average radiochemical yields of ^{18}F-THK-523, ^{18}F-THK-5105, ^{18}F-THK-5116, ^{18}F-THK-5117, and ^{18}F-FDDNP were 58%, 48%, 41%, 48%, and 22%, respectively. The specific activities of ^{18}F-labeded compounds ranged from 37 to 110 GBq/μmol, corrected at the end of synthesis. The mean specific activity of ^{11}C-PiB was 35 GBq/μmol.

In Vitro Binding Assays

The binding properties of phenylquinoline derivatives to tau fibrils was investigated and compared with Aβ1–42 fibrils. Although only a single class of ^{18}F-THK-5105 binding sites was identified on Aβ1–42 fibrils, 2 classes of ^{18}F-THK-5105 binding sites were identified on K18Δ280-tau fibrils. As shown in Table 2, the K_d for the first class of K18Δ280-tau binding sites was 1.45 nM, indicating higher binding affinity to tau fibrils than to Aβ1–42 fibrils (K_d = 35.9 nM). Further, competitive binding assays with ^{18}F-THK-5105 displayed high binding affinity of phenylquinoline derivatives to tau fibrils (Fig. 3). The K_i for THK-5117 was 10.5 nM, indicating that THK-5117 has higher binding affinity for tau fibrils than THK-523 (K_i = 59.3 nM). In contrast, the K_i for FDDNP was 263 nM. In binding assays using mesial temporal brain homogenates containing a high density of tau (1,075 pmol/g) and moderate density of Aβ (434 pmol/g), both ^{18}F-THK-5105 (K_d = 2.63 nM; B_{max} = 358 pmol/g of tissue) and ^{18}F-THK-5117 (K_d = 5.19 nM; B_{max} = 338 pmol/g of tissue) showed higher affinity for mesial temporal brain homogenates than ^{18}F-THK-523 (K_d = 86.5 nM; B_{max} = 647.1 pmol/g of tissue) (Supplemental Fig. 1; supplemental materials are available online only at http://jnm.snmjournals.org).

Tissue Staining and Autoradiography

The selective binding ability of the compounds was further examined using AD brain sections. The fluorescent compound THK-5105 clearly stained NFTs and neuropil threads in the hippocampal section of an AD patient (Fig. 4A). Selective binding of this compound with tau pathology was confirmed by comparing with the results of tau immunohistochemistry for the same sections (Fig. 4B). In contrast, SPs were faintly stained with THK-5105. Further, we compared findings of THK-5105 staining with those of Gallyas–Braak silver staining, a conventional technique used to visualize tau pathology in the AD brain (Figs. 4C and 4D), and the binding of THK-5105 to NFTs and neuropil threads was confirmed. The images of staining with THK-5116 and THK-5117 were similar to those with THK-5105 (data not shown).

To investigate the binding ability of ^{18}F-THK-5105 and ^{18}F-THK-5117 to NFTs at tracer doses, in vitro autoradiography was performed in postmortem AD brain sections, and the findings were compared with Gallyas–Braak staining and immunohistochemistry. In the mesial temporal sections, laminar distributions of ^{18}F-THK-5105 and ^{18}F-THK-5117 were observed in the deep layer of gray matter (Fig. 5A). A high density of tracer accumulation was observed in the CA1 area of the hippocampus, which is reported as the most frequent site for NFTs in AD (*31*). These tracer distributions coincided with Gallyas–Braak staining and tau immunostaining (Fig. 5B) but not with the distribution of ^{11}C-PiB (Fig. 5A) and Aβ immunostaining (Fig. 5B). In contrast, no significant accumulation of ^{18}F-THK-5105 and ^{18}F-THK-5117 was observed in the hippocampus of the healthy control subject (Supplemental Fig. 2). ^{18}F-THK-5116 failed to give a specific signal in the AD brain sections (data not shown).

To further assess the regional differences of tracer binding in the AD brain, ^{18}F-THK-5105 autoradiography was conducted using AD hemibrain sections and compared with the Aβ PET tracer ^{11}C-PiB (*32*). ^{18}F-THK-5105 densely accumulated in the gray matter of the hippocampus, parahippocampal gyrus, fusiform gyrus, inferior and middle temporal gyri, insula, and cingulate gyrus (Fig. 6A), regions known for the abundance of tau pathology in AD (*33*). In contrast, tracer binding in the parietal areas was modest. The pattern of tracer distribution correlated with the known distribution of tau pathology (Fig. 6A) but not with the known distribution of Aβ or the binding of ^{11}C-PiB (data not shown). In addition, quantitative analyses of these images demonstrated a significant correlation of ^{18}F-THK-5105 binding with tau immunostained areas but not with the areas of Aβ immunostaining (Fig. 6B; Supplemental Fig. 3). In contrast, ^{11}C-PiB bindings showed a good correlation with Aβ deposition but not with tau deposition (Supplemental Fig. 3).

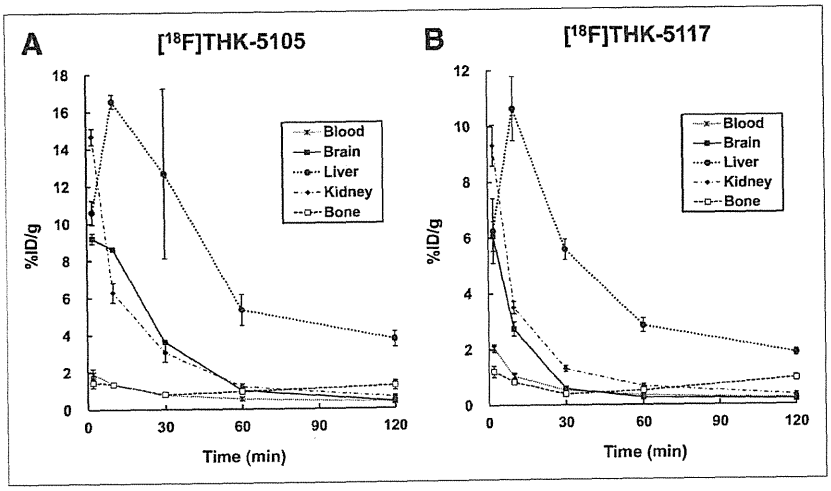

FIGURE 7. Time–activity curves after intravenous administration of ^{18}F-THK-5105 (A) and ^{18}F-THK-5117 (B) in mice.

Pharmacokinetics in Mice

All tested compounds exhibited sufficient amounts of tracer uptake in the mouse brain immediately after intravenous administration. Compared with ^{18}F-THK-523, new compounds showed significantly higher brain uptake at 2 min after injection (Table 1). ^{18}F-THK-5105 showed the highest brain uptake. In addition, clearance of these derivatives from normal brain tissue was faster than that of ^{18}F-THK-523 and ^{18}F-FDDNP (Table 1). The brain uptake ratio at 2 versus 60 min was highest for ^{18}F-THK-5117, followed by ^{18}F-THK-5105, ^{18}F-THK-5116, ^{18}F-FDDNP, and ^{18}F-THK-523. After injection of ^{18}F-THK-5105 and ^{18}F-THK-5117, the regional tracer uptake in the liver was highest at 10 min after injection, and the tracer was then slowly washed out from the body (Fig. 7). Compared with ^{18}F-THK-5105, ^{18}F-THK-5117 tended to have faster clearance from the brain, blood, liver, and kidney. No remarkable accumulation of ^{18}F-THK-5105 and ^{18}F-THK-5117 was observed in the bone.

Animal Toxicity Studies

A single intravenous administration of THK-5105 and THK-5117 at 1 mg/kg, equivalent to 100,000-fold the intended clinical dose for humans, caused no systemic toxicity in rats or mice. There were no unscheduled deaths or morbidity detected in this study. During the experimental period, the body weight of all animals increased normally, and no treatment-related changes were noted in any animals. There were no major clinical, biochemical, or histopathologic findings associated with the administration of THK-5105 and THK-5117.

Receptor Binding Assays

Binding inhibition of THK-5105 and THK-5117 was assessed in competitive radioligand binding assays against 60 common neurotransmitter receptors, ion channels, and transporters. As a result, no remarkable inhibition (<50%) was observed for various receptors, ion channels, and transporters at 1-μM concentrations of THK-5105 and THK-5117.

DISCUSSION

These findings suggest that ^{18}F-THK-5105 and ^{18}F-THK-5117 are promising candidates as tau imaging PET probes. Although previous saturation analysis showed the high binding affinity of ^{18}F-THK-523 for tau fibrils (K_d = 1.67 nM), the current competition assay demonstrated relatively lower binding affinity of THK-523 for tau fibrils (K_i = 59.3 nM) than THK-5105 (K_i = 7.8 nM) and THK-5117 (K_i = 10.5 nM). ^{18}F-THK-5105 showed higher affinity for tau pathology than for Aβ pathology in AD brain sections. Most amyloid imaging agents potentially bind to both tau and Aβ fibrils, because both protein fibrils share a common β-sheet secondary structure. To ensure the binding specificity of these compounds as tau-selective PET probes, the binding affinity to Aβ fibrils should be below the in vivo detection threshold. In vitro binding assays indicated that the binding affinity of ^{18}F-THK-5105 for Aβ fibrils (K_d = 35.9 nM) was 25 times lower than for tau fibrils (K_d = 1.45 nM). This K_d would allow selective detection of tau pathology, because the usual required K_d values for imaging Aβ are below 20 nM (*34*). However, the required K_d value for imaging tau deposits is still unknown. Considering that the concentrations of tau are about an order of magnitude lower than those of Aβ, the K_d value for tau should be well below 20 nM, in the low nanomolar range, to allow sensitive detection of tau pathology. In that respect, the binding affinities of both ^{18}F-THK-5105 and ^{18}F-THK-5117 to tau fibrils may be sufficient for in vivo detection of tau pathology in the brain. However, in vitro binding assay data should be carefully interpreted, because the structural conformation of synthetic tau fibrils does not fully correlate with the structure of NFTs and neuropil threads in the human brain. Actually, ^{18}F-THK-523 showed substantially lower affinity for AD brain homogenates (Kd = 86.5 nM) than for synthetic tau protein fibrils (Kd = 1.67 nM) (*15*). In the future, in vitro binding data should be compared with in vivo PET data to determine the required K_d value for in vivo tau detection.

In vitro assays using human brain samples are considered more reliable for evaluating the binding selectivity of radiotracers to tau and Aβ pathology at tracer doses. Autoradiography studies using human brain sections demonstrated the preferential binding of ^{18}F-THK-5105 and ^{18}F-THK-5117 to tau protein deposits in the AD brain. We observed a high density of ^{18}F-THK-5105 and ^{18}F-THK-5117 binding in the CA1 region of AD hippocampus, which contained substantial amounts of NFTs and neuropil threads. In addition, these tracers clearly visualized the laminar distribution of tau in the pri-α layer of the transentorhinal and temporal cortices, which is typically observed in the AD brain (*5*). The distribution pattern of THK tracer binding in AD brains was different from that of the Aβ imaging probe PiB and BF-227, which showed diffuse punctate distribution in broad neocortical gray matter and less tracer distribution in the mesial temporal region. These findings strongly suggest that binding properties of ^{18}F-THK-5105 and ^{18}F-THK-5117 are different from those of currently available Aβ PET probes. Compared with ^{18}F-THK-523 (*17*), both ^{18}F-THK-5105 and ^{18}F-THK-5117 showed higher contrast of tau pathology in autoradiographic images. These findings most likely reflect the increased binding affinity to tau by methylation of the amino group, as indicated by in vitro binding assays.

Similar findings were previously reported in an arylbenzothiazole derivative (*35*). Compared with ^{18}F-THK-5105, ^{18}F-THK-5117 showed lesser tracer binding in the gray matter containing high density of Aβ plaques, suggesting low binding affinity to Aβ and high selectivity to tau. ^{18}F-THK-5105 tends to show higher signals in the gray matter, and some of the images of ^{18}F-THK-5105 binding showed the patchy pattern as observed for ^{11}C-PiB binding. One possible reason for this is the binding of ^{18}F-THK-5105 to tau protein in dystrophic neurites. Another possible reason is binding of ^{18}F-THK-5105 to Aβ fibrils. However, the latter explanation seems unlikely given that ^{18}F-THK-5105 binding, as clearly shown in Figure 6, was correlated with tau, and not Aβ, deposits.

In vitro binding assays using AD brain homogenates are generally used to measure the binding affinity of Aβ imaging radiotracers to SPs or NFTs and the number of binding sites in real AD pathology (*36*). For most of the useful Aβ imaging radiotracers, the reported K_d or K_i values for neocortical brain samples are below 10 nM (*36,37*). In this study, the K_d values for high-affinity sites of AD mesial temporal homogenates were 2.63 nM for ^{18}F-THK-5105 and 5.19 nM for ^{18}F-THK-5117. These binding affinities were higher than that for ^{18}F-THK-523 and appear to be sufficient for the in vivo detection of AD pathology in the mesial temporal region at tracer doses. Furthermore, the B_{max}/K_d ratios of ^{18}F-THK-5105 and ^{18}F-THK-5117 for AD brain homogenates were 136.1 and 65.1, respectively, which fulfills the criteria (B_{max}/K_d ratio $>$ 10) for a good neuroimaging agent (*35*).

The optimization of pharmacokinetics is an important aspect in the development of a PET tracer (*38*). ^{18}F-THK-5105, ^{18}F-THK-5116, and ^{18}F-THK-5117 fulfilled the criteria of appropriate log P value (log P = 1–3) for brain entry (*39*). In mice, these tracers showed sufficient brain uptake and rapid washout from normal brain tissue. ^{18}F-THK-5105 and ^{18}F-THK-5117 exhibited high initial brain uptake in normal mice (>6 %ID/g at 2 min). These values, which are equivalent to over 100% injected dose index in a 25-g mouse, meet the prerequisites for useful PET imaging agents (*34*). The 2- to 60-min ratio of radioactivity concentrations for ^{18}F-THK-5117 was 23.1, indicating faster washout from normal brain for these compounds than for other currently available ^{18}F-labeled tracers such as ^{18}F-FDDNP (2.91), ^{18}F-florbetaben (4.83) (*40*), and ^{18}F-florbetapir (3.90) (*37*). Compared with ^{18}F-THK-523, ^{18}F-THK-5116 washed out faster from normal brain tissue of mice, indicating that the hydroxylation of the fluoroalkoxy group improves pharmacokinetics in mice. However ^{18}F-THK-5116 is not a suitable compound for clinical application, because of its lower initial brain uptake and binding affinity than the other 2 compounds.

CONCLUSION

^{18}F-THK-5105 and ^{18}F-THK-5117 should be considered as promising candidates for PET tau imaging radiotracers. Future clinical studies will clarify the usefulness of these radiotracers for the early detection of AD tau pathology.

DISCLOSURE

The costs of publication of this article were defrayed in part by the payment of page charges. Therefore, and solely to indicate this fact, this article is hereby marked "advertisement" in accordance with 18 USC section 1734. This study was supported by the research fund from GE Healthcare; the Industrial Technology Research Grant Program of the NEDO in Japan (09E51025a); Health and Labor Sciences Research grants from the Ministry of Health, Labor, and Welfare of Japan; and a Grant-in-Aid for Scientific Research (B) (23390297) and "Japan Advanced Molecular Imaging Program (J-AMP)" of the Ministry of Education, Culture, Sports, Science and Technology (MEXT), Japan. No other potential conflict of interest relevant to this article was reported.

REFERENCES

1. Organisation for Economic Co-operation and Development (OECD). *Understanding the Brain: The Birth of a Learning Science*. Paris, France: OECD Publishing, 2007.
2. Hardy J, Selkoe DJ. The amyloid hypothesis of Alzheimer's disease: progress and problems on the road to therapeutics. *Science*. 2002;297:353–356.
3. Lichtenberg B, Mandelkow EM, Hagestedt T, Mandelkow E. Structure and elasticity of microtubule-associated protein tau. *Nature*. 1988;334:359–362.
4. Holzer M, Holzapfel HP, Zedlick D, Bruckner MK, Arendt T. Abnormally phosphorylated tau protein in Alzheimer's disease: heterogeneity of individual regional distribution and relationship to clinical severity. *Neuroscience*. 1994;63:499–516.
5. Braak H, Braak E. Neuropathological stageing of Alzheimer-related changes. *Acta Neuropathol*. 1991;82:239–259.
6. Bondareff W, Mountjoy CQ, Roth M, Hauser DL. Neurofibrillary degeneration and neuronal loss in Alzheimer's disease. *Neurobiol Aging*. 1989;10:709–715.
7. Bobinski M, Wegiel J, Wisniewski HM, et al. Neurofibrillary pathology: correlation with hippocampal formation atrophy in Alzheimer disease. *Neurobiol Aging*. 1996;17:909–919.
8. Guillozet AL, Weintraub S, Mash DC, Mesulam MM. Neurofibrillary tangles, amyloid, and memory in aging and mild cognitive impairment. *Arch Neurol*. 2003;60:729–736.
9. Gómez-Isla T, Price JL, McKeel DW Jr., Morris JC, Growdon JH, Hyman BT. Profound loss of layer II entorhinal cortex neurons occurs in very mild Alzheimer's disease. *J Neurosci*. 1996;16:4491–4500.
10. Okamura N, Suemoto T, Furumoto S, et al. Quinoline and benzimidazole derivatives: candidate probes for in vivo imaging of tau pathology in Alzheimer's disease. *J Neurosci*. 2005;25:10857–10862.
11. Rojo LE, Alzate-Morales J, Saavedra IN, Davies P, Maccioni RB. Selective interaction of lansoprazole and astemizole with tau polymers: potential new clinical use in diagnosis of Alzheimer's disease. *J Alzheimers Dis*. 2010;19:573–589.
12. Ono M, Hayashi S, Matsumura K, et al. Rhodanine and thiohydantoin derivatives for detecting tau pathology in Alzheimer's brains. *ACS Chem Neurosci*. 2011;2:269–275.
13. Jensen JR, Cisek K, Funk KE, Naphade S, Schafer KN, Kuret J. Research towards tau imaging. *J Alzheimers Dis*. 2011;26(suppl 3):147–157.
14. Zhang W, Arteaga J, Cashion DK, et al. A highly selective and specific PET tracer for imaging of tau pathologies. *J Alzheimers Dis*. 2012;31:601–612.
15. Fodero-Tavoletti MT, Okamura N, Furumoto S, et al. ^{18}F-THK523: a novel in vivo tau imaging ligand for Alzheimer's disease. *Brain*. 2011;134:1089–1100.
16. Villemagne VL, Furumoto S, Fodero-Tavoletti MT, et al. The challenges of tau imaging. *Future Neurol*. 2012;7:409–421.
17. Harada R, Okamura N, Furumoto S, et al. Comparison of the binding characteristics of [^{18}F]THK-523 and other amyloid imaging tracers to Alzheimer's disease pathology. *Eur J Nucl Med Mol Imaging*. 2013;40:125–132.
18. Small GW, Agdeppa ED, Kepe V, Satyamurthy N, Huang SC, Barrio JR. In vivo brain imaging of tangle burden in humans. *J Mol Neurosci*. 2002;19:323–327.
19. Agdeppa ED, Kepe V, Liu J, et al. Binding characteristics of radiofluorinated 6-dialkylamino-2-naphthylethylidene derivatives as positron emission tomography imaging probes for beta-amyloid plaques in Alzheimer's disease. *J Neurosci*. 2001;21:RC189.
20. Thompson PW, Ye L, Morgenstern JL, et al. Interaction of the amyloid imaging tracer FDDNP with hallmark Alzheimer's disease pathologies. *J Neurochem*. 2009;109:623–630.
21. Tolboom N, Yaqub M, van der Flier WM, et al. Detection of Alzheimer pathology in vivo using both ^{11}C-PIB and ^{18}F-FDDNP PET. *J Nucl Med*. 2009;50:191–197.
22. Shoghi-Jadid K, Small GW, Agdeppa ED, et al. Localization of neurofibrillary tangles and beta-amyloid plaques in the brains of living patients with Alzheimer disease. *Am J Geriatr Psychiatry*. 2002;10:24–35.

23. Näslund J, Haroutunian V, Mohs R, et al. Correlation between elevated levels of amyloid beta-peptide in the brain and cognitive decline. *JAMA.* 2000;283: 1571–1577.
24. Mukaetova-Ladinska EB, Harrington CR, Roth M, Wischik CM. Biochemical and anatomical redistribution of tau protein in Alzheimer's disease. *Am J Pathol.* 1993;143:565–578.
25. Liu J, Kepe V, Zabjek A, et al. High-yield, automated radiosynthesis of 2-(1-{6-[(2-[^{18}F]fluoroethyl)(methyl)amino]-2-naphthyl}ethylidene)malononitrile ([^{18}F] FDDNP) ready for animal or human administration. *Mol Imaging Biol.* 2007;9:6–16.
26. Fodero-Tavoletti MT, Mulligan RS, Okamura N, et al. In vitro characterisation of BF227 binding to alpha-synuclein/Lewy bodies. *Eur J Pharmacol.* 2009;617:54–58.
27. Wilson AA, Garcia A, Chestakova A, Kung H, Houle S. A rapid one-step radiosynthesis of the beta-amyloid imaging radiotracer N-methyl-[C-11]2-(4′-methylaminophenyl)-6-hydroxybenzothiazole ([C-11]-6-OH-BTA-1). *J Labelled Comp Radiopharm.* 2004;47:679–682.
28. Cheng Y, Prusoff WH. Relationship between the inhibition constant (Ki) and the concentration of inhibitor which causes 50 per cent inhibition (IC50) of an enzymatic reaction. *Biochem Pharmacol.* 1973;22:3099–3108.
29. Okamura N, Suemoto T, Shimadzu H, et al. Styrylbenzoxazole derivatives for in vivo imaging of amyloid plaques in the brain. *J Neurosci.* 2004;24: 2535–2541.
30. Ikeda K, Akiyama H, Kondo H, Haga C. A study of dementia with argyrophilic grains. Possible cytoskeletal abnormality in dendrospinal portion of neurons and oligodendroglia. *Acta Neuropathol.* 1995;89:409–414.
31. Bouras C, Hof PR, Giannakopoulos P, Michel JP, Morrison JH. Regional distribution of neurofibrillary tangles and senile plaques in the cerebral cortex of elderly patients: a quantitative evaluation of a one-year autopsy population from a geriatric hospital. *Cereb Cortex.* 1994;4:138–150.
32. Kudo Y, Okamura N, Furumoto S, et al. 2-(2-[2-Dimethylaminothiazol-5-yl] ethenyl)-6- (2-[fluoro]ethoxy)benzoxazole: a novel PET agent for in vivo detection of dense amyloid plaques in Alzheimer's disease patients. *J Nucl Med.* 2007;48:553–561.
33. Braak H, Alafuzoff I, Arzberger T, Kretzschmar H, Del Tredici K. Staging of Alzheimer disease-associated neurofibrillary pathology using paraffin sections and immunocytochemistry. *Acta Neuropathol.* 2006;112:389–404.
34. Mathis CA, Wang Y, Klunk WE. Imaging beta-amyloid plaques and neurofibrillary tangles in the aging human brain. *Curr Pharm Des.* 2004;10:1469–1492.
35. Mathis CA, Wang Y, Holt DP, Huang GF, Debnath ML, Klunk WE. Synthesis and evaluation of ^{11}C-labeled 6-substituted 2-arylbenzothiazoles as amyloid imaging agents. *J Med Chem.* 2003;46:2740–2754.
36. Klunk WE, Wang Y, Huang GF, et al. The binding of 2-(4′-methylaminophenyl) benzothiazole to postmortem brain homogenates is dominated by the amyloid component. *J Neurosci.* 2003;23:2086–2092.
37. Choi SR, Golding G, Zhuang Z, et al. Preclinical properties of ^{18}F-AV-45: a PET agent for Abeta plaques in the brain. *J Nucl Med.* 2009;50:1887–1894.
38. Furumoto S, Okamura N, Iwata R, Yanai K, Arai H, Kudo Y. Recent advances in the development of amyloid imaging agents. *Curr Top Med Chem.* 2007;7:1773–1789.
39. Waterhouse RN. Determination of lipophilicity and its use as a predictor of blood-brain barrier penetration of molecular imaging agents. *Mol Imaging Biol.* 2003;5:376–389.
40. Zhang W, Oya S, Kung MP, Hou C, Maier DL, Kung HF. F-18 Polyethyleneglycol stilbenes as PET imaging agents targeting Abeta aggregates in the brain. *Nucl Med Biol.* 2005;32:799–809.

Eur J Nucl Med Mol Imaging (2013) 40:125–132
DOI 10.1007/s00259-012-2261-2

ORIGINAL ARTICLE

Comparison of the binding characteristics of [^{18}F]THK-523 and other amyloid imaging tracers to Alzheimer's disease pathology

Ryuichi Harada · Nobuyuki Okamura · Shozo Furumoto · Tetsuro Tago · Masahiro Maruyama · Makoto Higuchi · Takeo Yoshikawa · Hiroyuki Arai · Ren Iwata · Yukitsuka Kudo · Kazuhiko Yanai

Received: 1 May 2012 / Accepted: 21 September 2012 / Published online: 26 October 2012

Abstract
Purpose Extensive deposition of senile plaques and neurofibrillary tangles in the brain is a pathological hallmark of Alzheimer's disease (AD). Although several PET imaging agents have been developed for in vivo detection of senile plaques, no PET probe is currently available for selective detection of neurofibrillary tangles in the living human brain. Recently, [^{18}F]THK-523 was developed as a potential in vivo imaging probe for tau pathology. The purpose of this study was to compare the binding properties of [^{18}F]THK-523 and other amyloid imaging agents, including PiB, BF-227 and FDDNP, to synthetic protein fibrils and human brain tissue.
Methods In vitro radioligand binding assays were conducted using synthetic amyloid β_{42} and K18ΔK280-tau fibrils. Nonspecific binding was determined by the addition of unlabelled compounds at a concentration of 2 μM. To examine radioligand binding to neuropathological lesions, in vitro autoradiography was conducted using sections of AD brain.
Results [^{18}F]THK-523 showed higher affinity for tau fibrils than for Aβ fibrils, whereas the other probes showed a higher affinity for Aβ fibrils. The autoradiographic analysis indicated that [^{18}F]THK-523 accumulated in the regions containing a high density of tau protein deposits. Conversely, PiB and BF-227 accumulated in the regions containing a high density of Aβ plaques.
Conclusion These findings suggest that the unique binding profile of [^{18}F]THK-523 can be used to identify tau deposits in AD brain.

Keywords PET probes · Tau · Amyloid · Alzheimer's disease

Electronic supplementary material The online version of this article (doi:10.1007/s00259-012-2261-2) contains supplementary material, which is available to authorized users.

R. Harada · N. Okamura (✉) · S. Furumoto · T. Yoshikawa · K. Yanai
Department of Pharmacology,
Tohoku University School of Medicine,
2-1, Seiryo-machi, Aoba-ku,
Sendai 980-8575, Japan
e-mail: nookamura@med.tohoku.ac.jp

S. Furumoto · T. Tago · R. Iwata
Division of Radiopharmaceutical Chemistry,
Cyclotron and Radioisotope Center, Tohoku University,
Sendai, Japan

M. Maruyama · M. Higuchi
Molecular Imaging Center, National Institute
of Radiological Sciences,
Chiba, Japan

H. Arai
Department of Geriatrics and Gerontology, Institute of
Development, Aging and Cancer, Tohoku University,
Sendai, Japan

Y. Kudo
Innovation of New Biomedical Engineering Center,
Tohoku University,
Sendai, Japan

Introduction

Senile plaques and neurofibrillary tangles (NFTs) composed of amyloid-β (Aβ) peptides and aggregated tau proteins, respectively, are the pathological hallmarks of

Alzheimer's disease (AD). In vivo amyloid imaging techniques have received a lot of attention for their promise in presymptomatic detection of Aβ pathology [1]. Recently, several β-sheet binding radiotracers have been developed as PET amyloid imaging agents [2]. Among them, ^{18}F-labelled 2-(1-{6-[(2-fluoroethyl(methyl)amino)-2-naphthyl)ethylidene)malononitrile ([^{18}F]FDDNP) was the first PET probe to be applied to clinical PET imaging in patients with AD [3]. This tracer demonstrated higher regional uptake in the medial temporal lobe and neocortex, and was claimed to bind to Aβ and tau pathological lesions [3]. Subsequently, ^{11}C-labelled 2-[4′-(methylamino)phenyl]-6-hydroxybenzothiazole ([^{11}C]PiB) and 2-(2-[dimethylaminothiazole-5-yl]ethenyl)-6-(2-[fluoro]ethoxy)benzoxazole ([^{11}C]BF-227) were also developed as amyloid imaging radiotracers. These tracers bind to Aβ fibrils with high affinity [4] and have demonstrated a significantly higher retention in the neocortical areas of brains of AD patients than of healthy controls [5, 6]. Furthermore, post-mortem analysis of AD patients who had undergone [^{11}C]PiB PET imaging before death suggested a strong correlation between in vivo PiB binding and regional distribution of Aβ plaques [7].

Amyloid imaging with PET can detect AD pathology in its preclinical stage [8]. However, amyloid deposition as assessed by [^{11}C]PiB PET correlates poorly with cognitive impairment in AD [9, 10], whereas deposition of tau in the medial temporal cortex is closely associated with neuronal death in this region. Selective tau imaging would provide important information about the tau pathophysiological features in AD, allowing correlation of brain tau load with cognitive decline, monitoring of disease progression and evaluation of therapeutic efficacy of newly developed therapies. Potential candidates for in vivo tau imaging agents include quinoline derivatives [11], and in a recent study, we found that one quinoline derivative, [^{18}F]THK-523, showed higher affinity for tau rather than amyloid fibrils. Furthermore, an autoradiography analysis indicated that this tracer binds specifically to tau deposits but not Aβ burden at tracer concentrations usually achieved during a PET scan [12].

The binding profiles of PiB, BF-227 and FDDNP to Aβ fibrils have been well described. Because tau, α-synuclein and prion fibrils, as well as Aβ fibrils, share a common β-sheet secondary structure, these compounds can potentially bind all these misfolded proteins. A previous study indicated that PiB binds to both Aβ and PHF tau pathology in vitro [13]. However, the binding occurs at higher concentrations than usually achieved in vivo during a PET scan. Furthermore, PET–pathology correlation studies have demonstrated that PiB binding reflects Aβ pathology [7, 14]. Newly developed ^{18}F-labelled amyloid PET tracers have similarly shown good correlation with Aβ plaque density [15, 16]. However, the binding affinity of these radiotracers for tau fibrils remains unknown and the binding properties of [^{18}F]THK-523 have not been directly compared with those of other amyloid PET agents. Here, we compared the binding affinity of [^{18}F]THK-523 to synthetic Aβ and tau protein fibrils as well as to senile plaques and NFTs in human brain samples with those of PiB, BF-227 and FDDNP, to characterize the binding properties of THK-523 and to obtain a better understanding of current and future PET data.

Materials and methods

Materials

The nonlabelled compounds PiB, BF-227, FDDNP, THK-523 (Fig. 1) and their precursors were custom-synthesized by Tanabe R&D Service (Osaka, Japan). Human $A\beta_{42}$ was purchased from Peptide Institute Inc. (Mino, Japan). Recombinant K18ΔK280-tau protein was obtained from Invitrogen (Tokyo, Japan).

Radiolabelling of PiB, BF-227, THK-523 and FDDNP

[^{3}H]PiB (specific activity 2.96 GBq/μmol) was purchased from American Radiolabeled Chemicals (St. Louis, MO). [^{11}C]PiB was radiolabelled using its precursor (2-(4-aminophenyl)-6-methoxymethoxybenzothiazole) and [^{11}C]methyl triflate, as

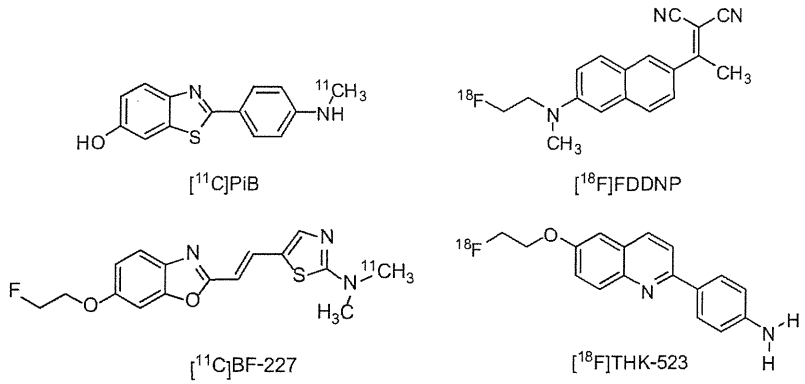

Fig. 1 Chemical structures of [^{11}C]PiB, [^{18}F]FDDNP, [^{11}C]BF-227 and [^{18}F]THK-523

previously described [17, 18]. The mean specific activity of [^{11}C]PiB was 34.6 GBq/μmol.

[^{18}F]BF-227 was synthesized by nucleophilic substitution of the tosylate precursor (2-[2-(2-dimethylaminothiazol-5-yl)ethenyl]-6-[2-(tosyloxy)ethoxy]benzoxazole. After a 10-min reaction at 110 °C, the crude mixture was partially purified on an activated Sep-Pak tC18 cartridge before being purified by semipreparative reverse-phase HPLC. Standard tC18 Sep-Pak reformulation produced [^{18}F]BF-227 in >95 % purity. The radiochemical yield was 12–19 % (non-decay-corrected), and the mean specific activity of [^{18}F]BF-227 was 163 GBq/μmol at the end of the synthesis. [^{11}C]BF-227 was synthesized using *N*-desmethylated derivatives as its precursor and [^{11}C]methyl triflate, as previously described [6]. The mean specific activity of [^{11}C]BF-227 was 136 GBq/μmol.

[^{18}F]THK-523 was synthesized by nucleophilic substitution of the tosylate precursor (2-(4-aminophenyl)-6-(2-tosyloxyethoxy)quinolone) as previously described [12]. The standard tC18 Sep-Pak reformulation produced [^{18}F]THK-523 in >95 % purity. The radiochemical yield was 38–49 % (non-decay-corrected), and the mean specific activity of [^{18}F]THK-523 was 68 GBq/μmol at the end of the synthesis.

[^{18}F]FDDNP was radiolabelled by the nucleophilic substitution of the tosylate precursor (2-{[6-(2,2-dicyano-1-methylvinyl)-2-naphthyl](methyl)amino}ethyl-4-methylbenzenesulphonate) as previously described [19]. After a 15-min reaction at 95 °C, the crude mixture was partially purified on an activated Sep-Pak tC18 cartridge before being purified by semipreparative reverse-phase HPLC. Standard tC18 Sep-Pak reformulation produced [^{18}F]FDDNP in >95 % purity. The radiochemical yield was 12–19 % (non-decay-corrected), and the mean specific activity of [^{18}F]FDDNP was 27 GBq/μmol at the end of the synthesis. All analysis HPLC chromatograms are shown in the Supplementary figure.

In vitro radioligand binding assays

Synthetic $A\beta_{42}$ fibrils and K18ΔK280-tau fibrils were prepared as previously described [12]. For in vitro binding assays, synthetic $A\beta_{42}$ or K18ΔK280 fibrils (200 nM) were incubated with increasing concentrations of [^{3}H]PiB and ^{18}F-labelled compounds (0.5–200 nM). To account for nonspecific binding of [^{3}H]PiB and ^{18}F-labelled compounds, the above-mentioned reactions were performed in triplicate in the presence of each unlabelled compound at a concentration of 2 μM.

The binding reactions were incubated for 1 h for the ^{18}F-labelled compounds and 3 h for [^{3}H]PiB at room temperature, in 200 μL of assay buffer (Dulbecco's PBS, 0.1 % BSA). Separation of bound from free radioactivity was achieved by filtration under reduced pressure (MultiScreen HTS Vacuum Manifold, MultiScreen HTS 96-well 0.65-μm filtration plate; Millipore, Billerica, MA). The filters were washed three times with 200-μL assay buffer, and the filters containing the bound ^{18}F-labelled compounds were then assayed for radioactivity in a γ counter (AccuFLEX γ7000, Aloka, Tokyo, Japan). The filters containing [^{3}H]PiB were incubated in 2 mL of scintillation fluid (Aquasol-2; PerkinElmer, Boston, MA), and the radioactivity of ^{3}H was counted using a β counter (LS6500 liquid scintillation counter; Beckman Coulter, Brea, CA). The binding data were analysed with curve-fitting software that calculated the K_D and B_{max} using nonlinear regression (GraphPad Prism version 5.0; GraphPad Software, San Diego, CA).

Autoradiography, immunohistochemistry and Gallyas silver staining

Demographics of post-mortem brain samples are shown in Table 1. The frontal and medial temporal brain sections (6 μm thick) of three AD patients were incubated with 1.0 MBq/mL ^{11}C-labelled and ^{18}F-labelled compounds at room temperature for 10 min and then washed briefly with water and 50 % ethanol. After drying, the labelled sections were exposed to a BAS-III imaging plate (Fuji Film, Tokyo, Japan) overnight. The autoradiographic images were obtained using a BAS-5000 phosphoimaging instrument (Fuji Film) with a spatial resolution of 25×25 μm. The adjacent sections were immunostained using AT8 anti-tau monoclonal antibody (diluted 1:20; Innogenetics, Ghent, Belgium) and 6F/3D (diluted 1:50; Dako, Glostrup, Denmark). The adjacent sections were also stained by the Gallyas-Braak method, which has been reported to be NFT-specific [20].

Results

Binding affinity for synthetic Aβ and tau fibrils

To characterize the binding properties of THK-523, PiB, BF-227 and FDDNP, in vitro radioligand binding assays for synthetic $A\beta_{42}$ and truncated tau construct (K18ΔK280) fibrils were performed under the same experimental conditions. Truncated tau construct (K18ΔK280) consists of the four repeat regions (244–372) but lacking lysine 280 (ΔK280) observed in FTLD-17 familial mutation.

Table 1 Demographics of brain samples used in this study

Brain no.	Age (years)	Sex	Post-mortem interval (h)
AD1	76	F	16
AD2	82	F	17
AD3	92	F	8.5

K18ΔK280 tau aggregates exhibit the similar characteristic as PHF-tau from AD brain [21]. In addition, K18ΔK280 tau forms aggregates quickly without cofactor such as heparin [22]. Thus, we used K18ΔK280 fibrils for the in vitro binding assays. Our analysis indicated that [^{18}F]THK-523 had a higher binding affinity for tau fibrils (K_{D1} = 1.99 ± 0.21 nM, B_{max1} = 1.22 ± 0.24 pmol THK-523/nmol K18ΔK280-tau) than for $A\beta_{42}$ fibrils (K_{D1} = 30.3 ± 3.91 nM, B_{max1} = 12.6 ± 0.45 pmol THK-523/nmol $A\beta_{42}$), which was similar to previously published data [12]. On the other hand, [^{3}H]PiB bound to $A\beta_{42}$ fibrils with high affinity (K_{D1} = 0.84 ± 0.18 nM, B_{max1} = 0.44 ± 0.07 pmol PiB/nmol $A\beta_{42}$). [^{3}H]PiB also showed two binding sites for K18ΔK280-tau fibrils, but with a lower affinity (K_{D1} = 6.39 ± 1.63 nM, B_{max1} = 1.38 ± 0.48 pmol PiB/nmol K18ΔK280) than [^{18}F]THK-523. [^{18}F]BF-227 showed a high binding affinity for $A\beta_{42}$ fibrils (K_{D1} = 1.72 ± 0.83 nM, B_{max1} = 0.50 ± 0.14 pmol BF-227/nmol $A\beta_{42}$), similar to our previous report [23], but showed a lower affinity for tau fibrils (K_D = 30.2 ± 2.29 nM, B_{max} = 10.7 ± 0.24 pmol BF-227/nmol K18ΔK280-tau). [^{18}F]BF-227 had an approximately 20-fold higher affinity for the first class of $A\beta_{42}$ binding sites compared with tau fibrils. Only one class of [^{18}F]FDDNP binding site was identified on the $A\beta_{42}$ (K_D = 5.52 ± 1.97 nM, B_{max} = 0.277 ± 0.06 pmol FDDNP/nmol $A\beta_{42}$) and K18ΔK280 tau fibrils (K_D = 36.7 ± 11.6 nM, B_{max} = 2.14 ± 0.46 pmol FDDNP/nmol K18ΔK280-tau). These results suggest that [^{18}F]FDDNP binds $A\beta_{42}$ fibrils with lower affinity than [^{3}H]PiB and [^{18}F]BF-227. Furthermore, [^{18}F]FDDNP had an approximately sevenfold higher affinity for $A\beta_{42}$ fibrils than for tau fibrils. These binding profiles are significantly different from that of [^{18}F]THK-523 (Table 2).

In vitro autoradiography of human brain sections

To further assess the binding selectivity of [^{18}F]THK-523, autoradiographic images of the frontal (Fig. 2) and medial temporal (Fig. 3) brain sections from three AD patients, using [^{18}F]THK-523, [^{11}C]PiB and [^{11}C]BF-227, were compared. While Aβ plaques in the frontal grey matter were labelled with [^{11}C]PiB (Fig. 2a–c) and [^{11}C]BF-227 (Fig. 2g–i), the binding of [^{18}F]THK-523 in the frontal grey matter (Fig. 2m–o) was considerably lower. In the medial temporal brain sections, [^{11}C]PiB (Fig. 3a–c) and [^{11}C]BF-227 (Fig. 3g–i) did not accumulate in the hippocampal CA1 area, whereas [^{18}F]THK-523 (Fig. 3m–o) did accumulate in this area (Fig. 3m–o). The presence of a high density of tau and a low density of Aβ in this area was confirmed by immunohistochemistry (Fig. 3d–f, j–l). Furthermore, the band-like distribution of [^{18}F]THK-523 in the inner layer of the temporal grey matter was similar to the distribution of tau (Fig. 3j–l). In the high-magnification images of case AD3 (Fig. 3p–v), the distribution of [^{18}F]THK-523 closely resembled Gallyas silver staining and tau immunostaining. [^{18}F]THK-523 binding was observed in the areas showing a high density of NFTs in the hippocampal CA1, the layer pre-α and pri-α in the entorhinal cortex (ERC) (Fig. 3p, q, r, t). Intriguingly, [^{18}F]THK-523 labelling in the layer pre-α of the ERC corresponded to Gallyas silver staining better than tau immunostaining, suggesting the preferential binding of [^{18}F]THK-523 to extracellular tau deposits that were clearly visualized by Gallyas silver staining [25]. In contrast to [^{18}F]THK-523, the distribution of [^{11}C]PiB was similar to that of Aβ immunohistochemistry (Fig 3q, u, v). [^{11}C]PiB binding corresponded to the formation of amyloid in the parvopyramidal layer of the presubicular area and in the layers pre-β and pre-γ of the ERC (Fig. 3s, v) [26].

Discussion

In the study reported here, we for the first time directly compared the binding properties of the novel quinoline derivative THK-523 and other amyloid PET probes. Our data suggest the potential utility of THK-523 for the selective detection of PHF-tau in the living human brain, which has not previously been achieved. The autoradiographic images of sections from AD brains revealed that [^{18}F]THK-523 successfully labelled PHF-tau deposits but did not label Aβ deposits in the frontal and temporal cortices. These findings suggest that [^{18}F]THK-523 is a promising

Table 2 K_D and B_{max} values of [^{3}H]PiB, [^{18}F]BF-227, [^{18}F]FDDNP and [^{18}F]THK-523 for K18ΔK280-tau and $A\beta_{42}$ fibrils

Compound	K18ΔK280 fibrils				$A\beta_{42}$ fibrils			
	K_{D1}	B_{max1}	K_{D2}	B_{max2}	K_{D1}	B_{max1}	K_{D2}	B_{max2}
[^{18}F]THK-523	1.99±0.21	1.22±0.24	50.7±2.73	4.55±0.74	30.3±3.91	12.6±0.45	–	–
[^{18}F]BF-227	30.2±2.29	10.7±0.24	–	–	1.72±0.83	0.50±0.14	56.1±25.1	13.4±4.37
[^{18}F]FDDNP	36.7±11.6	2.14±0.46	–	–	5.52±1.97	0.277±0.06	–	–
[^{3}H]PiB	6.39±1.63	1.38±0.48	304±77.4	20.6±11.2	0.84±0.18	0.44±0.07	60.6±8.32	26.1±8.57

K_D values are in nanomoles, and B_{max} values are in picomoles compound per nanomole fibrils (n=3).

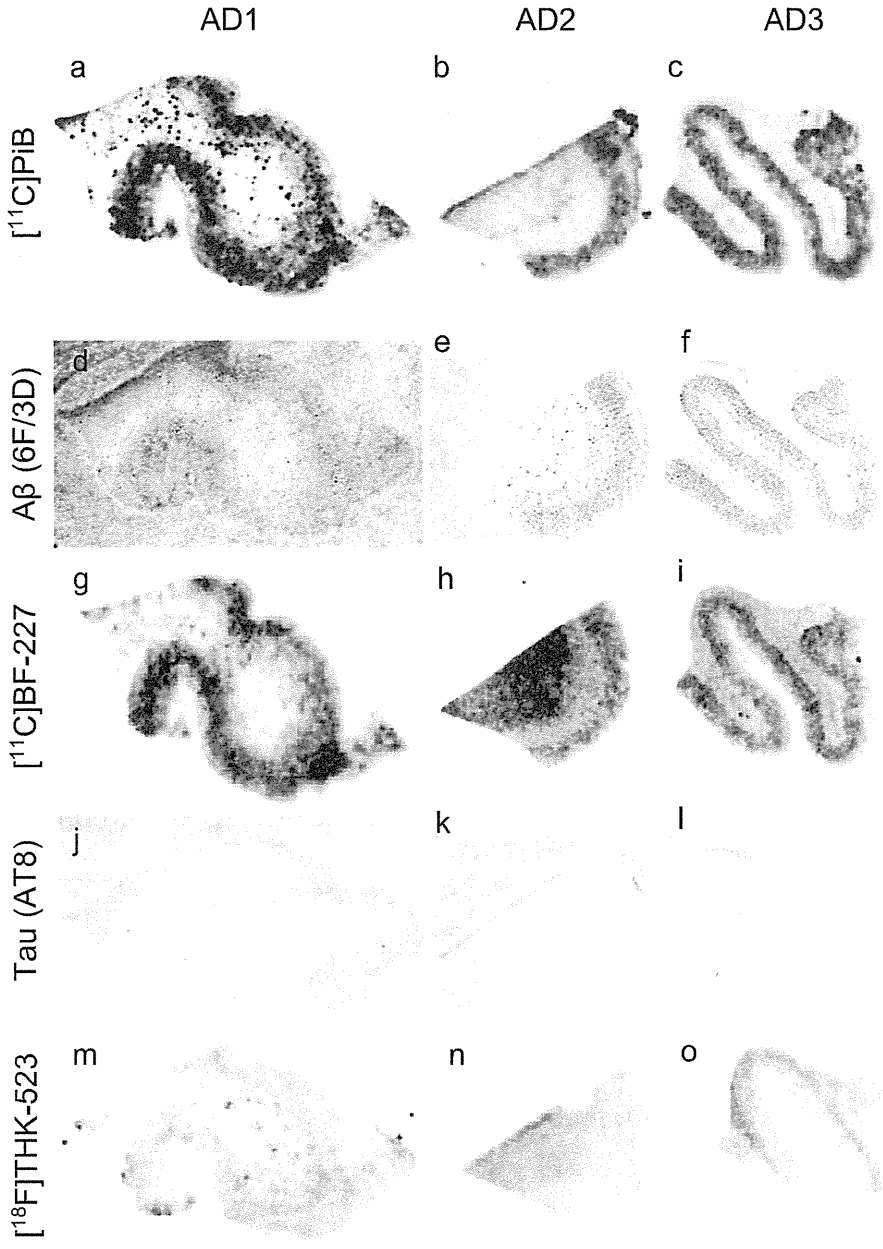

Fig. 2 Comparison of [^{11}C]PiB, [^{11}C]BF-227 and [^{18}F]THK-523 autoradiography with the Aβ and tau immunostaining in sections of the frontal brain from three patients with AD (*AD1*, *AD2*, *AD3*). Both [^{11}C]PiB (**a–c**) and [^{11}C]BF-227 (**g–i**) showed dense accumulation in the grey matter, closely resembling the pattern of Aβ immunohistochemistry using the 6F/3D antibody (**d–f**). [^{18}F]THK-523 (**m–o**) did not accumulate in the grey matter, which was correlated with no marked staining with anti-tau antibody AT8 (**j–l**)

candidate as a tau imaging tracer, and could also be a lead compound for future development of tau-selective radiotracers. We speculate that [^{18}F]THK-523 would show retention in tau-rich brain regions if administered to AD patients. However, the specific signal of [^{18}F]THK-523 might be lower than those of PiB and BF-227 owing to the lower amount of tau deposits in the neocortex of AD patients [27]. Further compound optimization may be required to achieve higher contrast imaging of PHF-tau deposits.

In in vitro saturation binding studies [^{18}F]THK-523 bound with higher affinity to tau fibrils (K_{D1} 1.99 nM) than to $A\beta_{42}$ fibrils (K_{D1} 30.3 nM), whereas PiB and BF-227 showed the opposite binding characteristics. [^{3}H]PiB bound with higher affinity to $A\beta_{42}$ fibrils (K_{D1} 0.84 nM) than to tau fibrils (K_{D1} 6.39 nM), similar to previous reports [7, 28, 29], and [^{18}F]BF-227 had more than a tenfold higher affinity for $A\beta_{42}$ fibrils (K_{D1} 1.72 nM) than for tau fibrils (K18ΔK280; K_{D1} 30.2 nM). Autoradiographic images of sections of AD brain revealed that [^{11}C]PiB and [^{11}C]BF-227 accumulated in the grey matter of the neocortex, which closely resembled the staining pattern of Aβ immunohistochemistry. A previous study suggested that [^{3}H]PiB labelled NFTs at tracer concentrations usually achieved during a PET scan [13]. However, another study showed no binding of the PiB derivative [^{3}H]BTA-1 to